Using inverse imaging in the thermal modelling of LPBF processes for domains with circular boundaries

Msc. Thesis

Marouan Oulad Si Omar

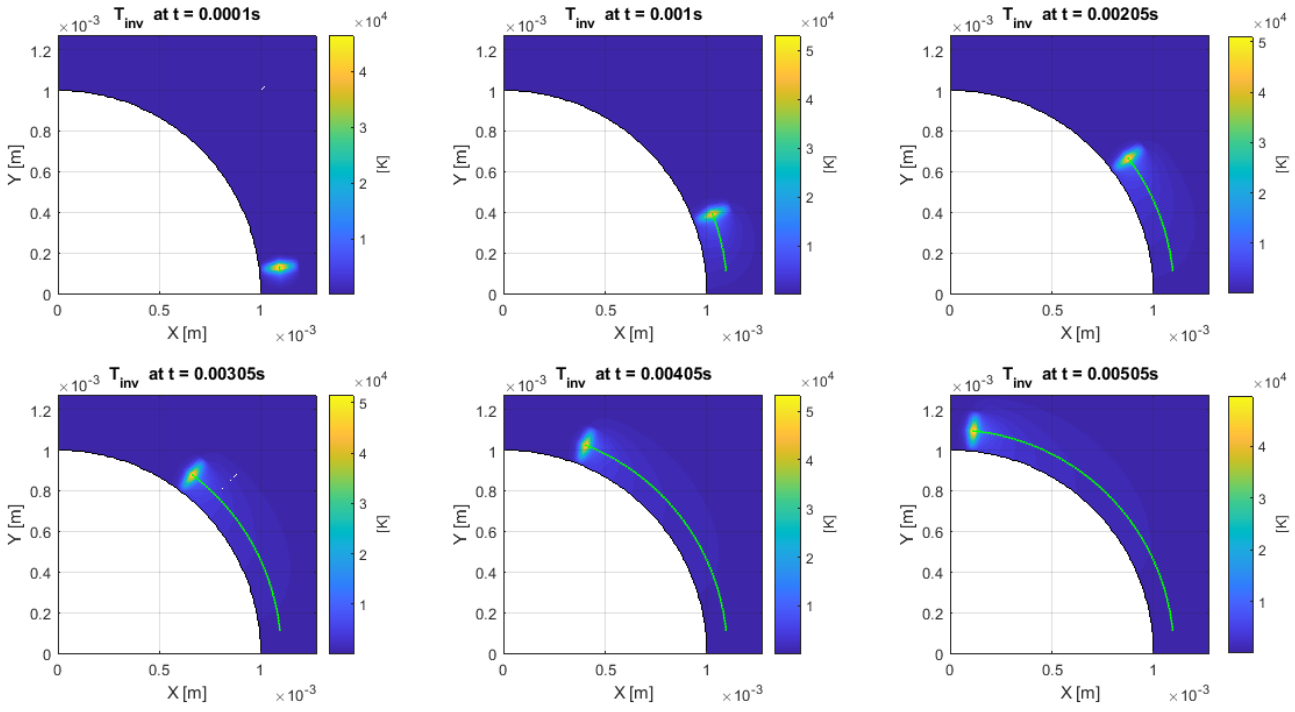

TU Delft

Using inverse imaging in the thermal modelling of LPBF processes for domains with circular boundaries

by

Marouan Oulad Si Omar

Student number:	4303474
Instructor:	C. Ayas
Teaching Assistant:	Y. Yang
Date:	15 May, 2024
Specialisation:	Structural Optimisation and Mechanics
Faculty:	Faculty of Mechanical, Maritime and Materials Engineering, Delft

TU Delft

Acknowlegdements

With the completion of this thesis I conclude my wonderful time I had at the TU Delft. I want to take the opportunity to thank the people who supervised and supported me.

I would like to thank my supervisor Dr. Can Ayas for his helpful supervision and insights. I especially admired his trust in my autonomy to manage my thesis and his co-equal treatment even as a supervisor. I felt myself free to explore the topics I was interested in. I also want to than Yang for his useful feedback during the course of the thesis writing and support. He was always available when needed.

Last but surely not least, I want to thank my family, my both parents, my brothers and sisters, and my friends for motivating me, giving me hope and supporting me in a way, no other humans could do.

Marouan Oulad Si Omar
Delft, May 2024

Summary

In this thesis a new efficient model has been developed in the thermal analysis of Laser Powder Bed Fusion, an Additive Manufacturing (or: 3D-printing) method that is used to manufacture metal products. During this process, a laser is used as a heat source to melt metal powder grains to each other, that are solidified when cooled down. In Laser Powder Bed Fusion high temperatures changes arise at the laser spot, that are in a scale smaller than the scale of the manufactured product. This requires a very fine spatial discretization (or: mesh) if the thermal analysis is done purely numerical. A fine mesh leads to high computational cost. Various methods have been previously developed to reduce this costs, like the semi-analytic method. The new model in this thesis is based on a the previously developed thermal model that uses the semi-analytic method.

In the semi-analytic approach a clever method has been developed to reduce the computational costs of numerical thermal simulation, by adding a specifically chosen analytic solution to the numerical solution in the thermal modelling of Laser Powder Bed Fusion. This analytic solution is chosen such that the numerical solution is allowed to use a coarser mesh, and thus reduces the computational costs. The reduction of computational costs is due to a mathematical tool, called the method of images, that is used in this analytic solution. If the product that is manufactured by Laser Powder Bed Fusion has planar boundaries, the method of images provides a high computational efficiency, as is shown by previous researches. However, for products with circular boundaries, the method of images is not so efficient as it is for planar boundaries. Therefore, another method has been developed for circular boundaries that uses a certain scaling factor, a modulation, in the method images. In this thesis another approach than modulation has been developed, in the search of a more efficient method than modulation. This is done by using a different method of imaging, namely inverse imaging, that is inspired by the solution in electrostatics for domains with circular boundaries.

The new model in this thesis uses an analytic solution with inverse imaging. This analytic solution is meant to be used in the semi-analytic modelling for thermal analysis in Laser Powder Bed Fusion. A key criteria that makes an analytic solution appropriate for the semi-analytic method is that the boundary fluxes of the analytic solution are smooth enough. The boundary fluxes are namely the input for the numerical solution that is used in the semi-analytic method. In order for this numerical solution to capture the behaviour of the boundary flux of the analytical solution, the spatial discretization should be fine enough. A smooth boundary flux can be captured numerically by a coarser mesh, contrary to a boundary flux with steep peeks, that requires a finer mesh. A finer mesh is thus computationally less efficient.

The results in this thesis show that inverse imaging gives a smoother flux for circular boundaries than the previously developed model that uses modulation. This is due to the fact that the heat flux is reflected better through the circular boundary when inverse imaging is used. This better reflection is caused by the geometrical parameters inspired from electrostatics. As a result of the better smoothness of inverse imaging, a coarser mesh can be used in the numerical solution when the semi-analytic method is applied, and thus the computational costs can be reduced. Therefore, this thesis shows that for the thermal modelling of Laser Powder Bed Fusion with circular boundaries, inverse imaging is more appropriate to be used in the semi-analytic method than modulation.

Contents

1 Introduction

Manufacturing has been important in the life of human beings throughout history. Civilizations have been developing manufacturing methods until today, and will continue to do that. One of the breakthroughs in the history of manufacturing is a method called Additive Manufacturing (AM), where products are produces layer by layer.

AM has various methods depending on the material that is used. For metals the AM method used is called Laser Poweder Bed Fusion (LPBF). In LPBF each layer is produced by scanning a laser on a metal powder bed at selected positions. As a result of the heat produced by the laser, the metal powder melts and then solidifies, creating a solid metal part. This is done layer by layer. During this process, the manufactured product undergoes thermal extensions and contractions. As a result of these extensions and contractions stresses are built up in the metal part. These stresses are called residual stresses. The load resistance can be limited by residual stresses [1].

In manufacturing, determining the load resistance is important. To reduce the residual stresses, process parameters like the laser scan velocity or the power of the laser have to be optimized. To avoid expensive physical experiments, models are developed that can provide much information without wasting any material. However, to develop a model that is both accurate and computational efficient can be a challenging task, especially for LPBF-processes. This is mainly because during the manufacturing process the laser causes a steep temperature change on a laser spot radius that is much smaller than the scale of the manufactured product. In order to catch the thermal behaviour within the product caused by the heating laser source, the mesh size in the spatial discretization has to be very fine, which leads to high computational costs.

Without giving much detail at this point in the thesis, one way to reduce the computational cost is to use the semi-analytic method for the thermal modelling [2,3]. Various improvements of this method have been made, such as using the method of (equidistant) images for planar boundaries. This method however does not work very well on circular boundaries. Therefore, for circular boundaries an improvement of the method of (equidistant) images has been made, that uses a certain modulation [4]. All these methods will be explained throughout this thesis in great detail.

Although several methods have been developed, improvement is still needed in the thermal analysis of circular boundaries, in order to reduce the computational cost more. Therefore, in this thesis a new method will be explored, that makes use of 'inverse imaging', as will be explained later. The main question that will be answered is: 'How appropriate is inverse imaging in the semi-analytic thermal modelling of LBPF-processes for circular boundaries compared to modulated equidistant imaging method?' This research question will be explored step wise.

First, in chapter 2 the relevant background knowledge will be given. This will be done by explaining what the LBPF-process exactly is and how thermal analysis is done for this process. Furthermore, the semi-analytic method will be introduced and its advantages will be explained. Also, the application of

the semi-analytic method on circular boundaries, by the use of a modulation method will be shown. This will be the basis in understanding the state of the art of how the semi-analytic method is applied in the thermal modelling of LBPF-processes for domains with circular boundaries. After that, inspiration from the field of electrostatics will be sought, where inverse imaging is used to solve problems in domains with circular boundaries.

After understanding the semi-analytic method in thermal modelling and knowing how inverse imaging is applied in electrostatics, the methodology to answer the main question will be explained in details in chapter 3. The problem description will be given and eventually the new model will be shown that uses inverse imaging.

In chapter 4 the inverse imaging will be compared to the modulation method that is taken from the state of the art. The results will be shown and discussed. Conclusions will be drawn in chapter 5 based on the results obtained from the previous chapter. After that relevant recommendations on future research will be made.

2
Background

In this chapter relevant background information will be given in order to understand the relevance of developing a new model for the thermal analysis of Laser Powder Bed Fusion. Having read this chapter, one will understand where the interest of using inverse imaging comes from.

First, an explanation will be given on Additive Manufacturing in general and Laser Bed Powder Fusion in specific. After that the necessity of thermal models in Laser Bed Powder Fusion will be shown. Then, the mathematical and physical basics of the analysis in thermal modeling will be laid out by explaining the governing equation, the heat equation, and how it is solved analytically and numerically. This will bring us eventually to a very elegant and efficient method of solving the heat equation for Laser Bed Powder Fusion processes, called the semi-analytic method. Both the advantages and limitations of the semi-analytic method will be explained in detail.

For planar boundaries, the semi-analytic method can be made computationally efficient by applying a specific method called the method of images, as will be explained. However, for circular boundaries the method of images does not give the computational efficiency like it gives for planar boundaries. This makes circular boundaries in the semi-analytic method for thermal analysis an important topic of research. We will therefore discuss in this chapter one of the attempts that have been made for thermal analysis, namely improving the the method of images by using a certain modulation.

Reading the mentioned topics in this chapter, the reader will have a clear vision of the state of the art of applying the semi-analytic method for circular boundaries in LPBF-processes. In this thesis the aim is to find another method that works better for the method of images than modulation. Therefore, at the end of this chapter inspiration in the field of electrostatics will be sought, since electrostatics uses a different method of imaging than in thermal analysis, namely inverse imaging, for solving problems with circular boundaries.

2.1. Additive Manufacturing and Laser Powder Bed Fusion

Additive Manufactuting or 3D printing contains all production processes in which a product is built by adding material layer by layer. AM is much more advantageous than traditional manufacturing methods like moulding or machining. One of the advantages of AM is that complex shapes can be produced, that could not have been made by traditional manufacturing methods [5]. This makes it possible for designers to produce a single part with a complex shape for integrated functionalities, that previously required separate parts. Another advantage of AM is the possibility to customize and personalize products in low volumes for moderate costs. Also decentralization of the manufacturing process is possible: one can make a product at every location and time. A key advantage of AM is that during the most AM-manufacturing processes the material is added where it is needed, which results in reduction of waste material [5].

AM has different methods for various material classes, as is illustrated in figure 2.1. One of them is

Laser Powder Bed Fusion , also known as Selective Laser Melting, that is used for metals. In LPBF a laser is pointed to a layer of metal powder and is utilized as a heat source. While the laser scans the powder, the metal powder melts along the laser path, bonds with each other and then solidifies when it cools down. The laser only scans the powder at the regions where one wants to produce the desired product. When a layer of metal powder is scanned by the laser at the desired regions, the next layer of powder is placed above the previously produced layer. Then the process starts all over again, until the product is fully manufactured layer by layer. In this thesis, we will dive more in the thermal modelling of the LPBF-process. Studying the thermal modelling of LPBF-processes can lead to improvements of the process, as will be discussed next.

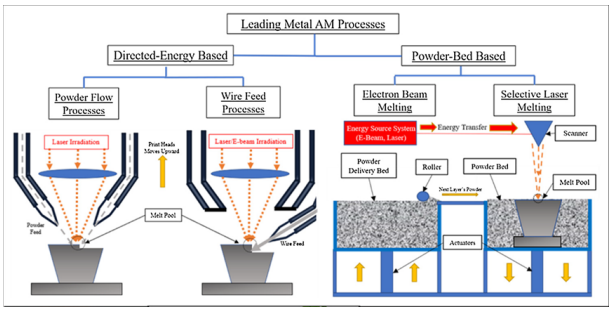

Figure 2.1: Note. Reprinted from "Invited review article: Metal-additive manufacturing - Modeling strategies for application-optimized designs," by A. Bandyopapadhyay & Kellen D. Traxel, 2018 [7].

2.2. The necessity of the thermal modelling of the LPBF-process

Predicting the load resistance of a product that is manufactured in a LPBF-process, gives insight about the product quality and about improving the the LPBF- process. These predictions are not only based on experiments but also on mathematical and physical models. These models are largely dependent or focused on the thermal behaviour inside the manufactured product during the LPBF-process. The thermal behaviour is namely very critical in LPBF-processes, since the laser causes a very high temperature rise at the spot it is pointed to. The heat that is released is conducted from the laser spot to the rest of the product. However it takes time for the heat to get diffused in the product, which leads to temperature differences inside the product during the LPBF-process. As a consequence of these temperature changes and differences, large deformations and residual stresses occur during the manufacturing process [6]. This can lead to a reduction in the load resistance of the product and thermal cracks can be formed. Also the porosity inside the product can vary [2]. All these are consequences of the thermal behaviour inside the product during the manufacturing process. Thus thermal modelling is key in predicting and optimizing the product quality in LPBF.

2.2.1. Numerical models

Most of the models that are used to do the thermal analysis are numerical models, especially Finite Element models . However, modelling the laser by Finite Elements (or any other numerical method) can be computationally very inefficient, because of the fine mesh that is required to capture the thermal behaviour around the laser spot. The laser namely causes a large temperature rise over a laser spot radius, that is much smaller than the remaining domain of the product [2, 3]. More details about how the mesh size influences the computational cost will be discussed later in this chapter.

2.2.2. Semi-analytic models

There is a method used in LPBF-processes that can reduce the high computational costs caused by the numerical modelling of the laser, called the semi-analytic method [2, 3]. In this method, the laser is not modelled numerically. Instead an analytic solution for a point source in infinite or semi-infinite space is used to model the laser. However, during the LPBF-proces, most boundaries of the product are modelled as insulated boundaries, and thus require a model that fulfill the boundary conditions of an insulated boundary. The mentioned analytic solution does not fulfill these boundary conditions, since it is in infinite of semi-infinite space. Therefore, a numerical field is introduced in the semi-analytic method that uses the complementary boundary fluxes of the analytic solution. When the analytic and

numerical field are added up, the boundary fluxes of the total field are zero, which fulfills the insulated boundary conditions. Also, when adding the two field up, the behaviour of the laser is taken into account by the analytic field, and since the laser is not modelled numerically a coarser mesh is allowed in the numerical field [2, 3]. More details about the semi-analytic method will be explained later in this chapter.

The semi-analytic method works good for planar boundaries [2, 3], by allowing the numerical field to have a coarser mesh. This is mainly caused by the fact that the method of images is used in the analytic field. The method of images forces the analytic field to have a zero flux at planar boundaries by modelling an image source outside the domain [2, 3], as shall be discussed later. For circular boundaries, the method of images does not give a zero flux along the boundary, as will explained in this chapter. However there is a method developed that modifies the method of images, by modulating the image source by a specific factor [4], as will come near the end of the chapter.

Circular boundaries arise a lot in products that are manufactured by LPBF. In this thesis, the aim is to search for an analytic solution that is more appropriate for circular boundaries than the mentioned model that uses modulation. This will be done by investigating how boundary conditions are fulfilled for circular boundaries in fields outside heat conduction, especially electrostatics. To understand why this approach is taken, it is important to know what the limitations are in the analytic and numerical modelling in thermal analysis. It is also important to know what the limitations are of the semi-analytic method for circular boundaries, and why a more suiting approach than modulation in the semi-analytic method is desired. These topics will be explained in the remainder of this chapter. But first, it is important to understand the basics of thermal analysis, by understanding the governing equation in thermal analysis.

2.3. The governing equation

The heat equation is the governing equation in thermal analysis. Gaining insight about the heat equation is the starting point of understanding how to improve the thermal modelling of the LPBF-processes. Therefore, a short derivation based on energy balances will be given and the types of boundary conditions that can occur in heat conduction will be explained. After that, a brief discussion will be held about solving the heat equation.

2.3.1. Derivation of the heat equation

The thermal energy of a system E_{system} is the energy as a result of the vibration and motion of it's molecules. The higher the temperature is in a system, the higher the thermal energy will be. The rate of thermal energy in the volume V of the system is given by the energy heat equation:

$$\frac{dE_{\text{system}}}{dt} = \int_V c_p \rho \frac{\partial T(\mathbf{x}, t)}{\partial t} d\Omega \,, \tag{2.1}$$

where T is the temperature, $\mathbf{x}$ is the position vector that contains the spatial coordinate variables ((x, y, z) in Cartesian coordinates), t is the time variable, c_p is the thermal capacity and ρ is the material density. The integration is done over the volume V of the system using the dummy variable Ω.

The heat flux $\mathbf{q}$ is defined by the rate of energy transfer through the surface S of the system. The total energy that enters or leaves the system through the surface is:

$$\frac{dE_{\text{surface}}}{dt} = \int_S \mathbf{q} \cdot \mathbf{n} d\Gamma \,, \tag{2.2}$$

where Γ is the dummy variable that is used to integrate over the surface S of the system and $\mathbf{n}$ is the normal vector that is outer to the surface. By using the divergence theorem [11], this equation can be rewritten as:

$$\frac{dE_{\text{surface}}}{dt} = \int_S \mathbf{q} \cdot \mathbf{n} d\Gamma = \int_V \nabla \cdot \mathbf{q} d\Omega \,. \tag{2.3}$$

If an internal heat source or forcing term is present, the energy that is generated is given by:

$$\frac{dE_{\text{internal}}}{dt} = \int_V Q d\Omega \,, \tag{2.4}$$

where Q is the volumetric internal heat generation. In figure 2.2 an illustration of the system is given.

The energy of the system is a balance of the energy of the heat source and the energy that passes through the surface of the system:

$$\begin{aligned} \frac{dE_{\text{system}}}{dt} &= \frac{dE_{\text{internal}}}{dt} - \frac{dE_{\text{surface}}}{dt} \\ \int_V c_p \rho \frac{\partial T}{\partial t} d\Omega &= \int_V (Q - \boldsymbol{\nabla} \cdot \mathbf{q}) d\Omega \,. \end{aligned} \tag{2.5}$$

This gives:

$$\int_V (c_p \rho \frac{\partial T}{\partial t} + \boldsymbol{\nabla} \cdot \mathbf{q} - Q) d\Omega = 0 \,. \tag{2.6}$$

Because this integral is zero for every volume V, the local form of the equation is:

$$c_p \rho \frac{\partial T}{\partial t} + \boldsymbol{\nabla} \cdot \mathbf{q} - Q = 0 \,. \tag{2.7}$$

Heat flows by means of conduction in solid volumes. Heat flux by conduction is described by Fourier's law:

$$\mathbf{q} = -k \boldsymbol{\nabla} T \,, \tag{2.8}$$

were k is the thermal conductivity. This gives us the following expression:

$$c_p \rho \frac{\partial T}{\partial t} - \boldsymbol{\nabla} \cdot (k \boldsymbol{\nabla} T) - Q = 0 \,, \tag{2.9}$$

or:

$$c_p \rho \frac{\partial T}{\partial t} = \boldsymbol{\nabla} \cdot (k \boldsymbol{\nabla} T) + Q \,. \tag{2.10}$$

This is expression is called the heat equation. In this thesis for simplicity it is assumed that the material properties c_p, ρ and k are isotropic, constant and linear. Therefore we will rewrite the heat equation as:

$$\frac{\partial T}{\partial t} = \alpha \nabla^2 T + \frac{Q}{c_p \rho} \,, \tag{2.11}$$

where the diffusivity α is defined as:

$$\alpha = \frac{k}{c_p \rho} \,. \tag{2.12}$$

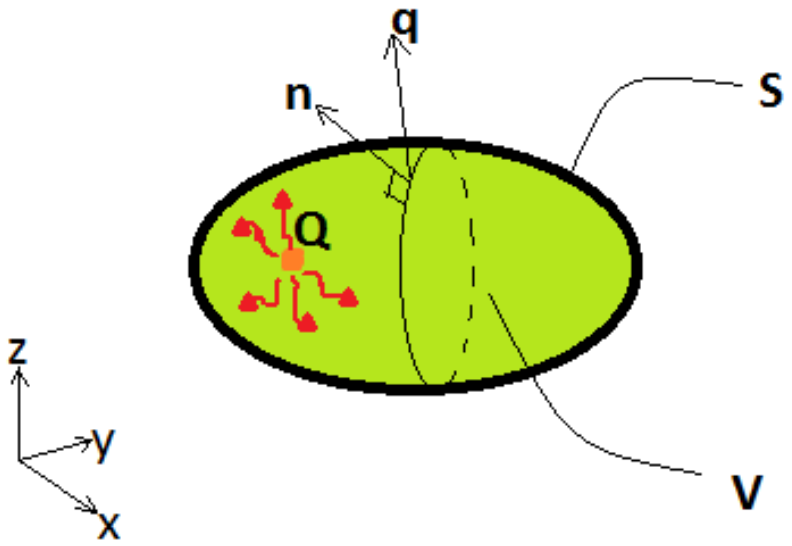

Figure 2.2: Illustration of the system.

2.3.2. Initial and boundary conditions

Besides the governing equation, the initial and boundary conditions determine how the temperatures and fluxes behave in the system. The initial condition $T_0(\mathbf{x})$ is the temperature field at the time $t = t_0$:

$$T_0(\mathbf{x}) = T(\mathbf{x}, t_0)\,. \tag{2.13}$$

Three possible boundary conditions that a system can have in heat transfer problems [8, 9] will be discussed:

1. For Dirichlet or temperature boundary condition the surface has a prescribed temperature T_s: $T(\mathbf{x}, t) = T_s(\mathbf{x}, t)$, $\mathbf{x} \in \partial\Omega$.
2. For Neumann or flux boundary condition the surface has a prescribed normal flux q_s. The boundary conditions are: $-k\frac{\partial T}{\partial \mathbf{n}} = -k\nabla T(\mathbf{x}, t) \cdot \mathbf{n} = q_s(\mathbf{x}, t)$, $\mathbf{x} \in \partial\Omega$.
3. For convective boundary condition the normal flux, boundary temperature and the fluid temperature T_{fluid} have the following relationship: $k\frac{\partial T}{\partial \mathbf{n}} = h(T(\mathbf{x}, t) - T_{\text{fluid}})$, $\mathbf{x} \in \partial\Omega$. Here h is the heat transfer coefficient. There is a similar boundary condition to convective called radiation boundary conditions. For the radiation boundary condition the normal flux, boundary temperature and the ambient temperature T_{ambient} have the following relationship: $k\frac{\partial T}{\partial \mathbf{n}} = \beta\kappa_B(T(\mathbf{x}, t)^4 - T_{\text{fluid}}^4)$, $\mathbf{x} \in \partial\Omega$. Here β is the emmisivity coefficient and κ_B is the Stephan-Boltzmann constant ($5.67032 \times 10^{-8} \text{W/m}^2/\text{K}^4$) [8, 9].

These boundary conditions are illustrated in figure 2.3.

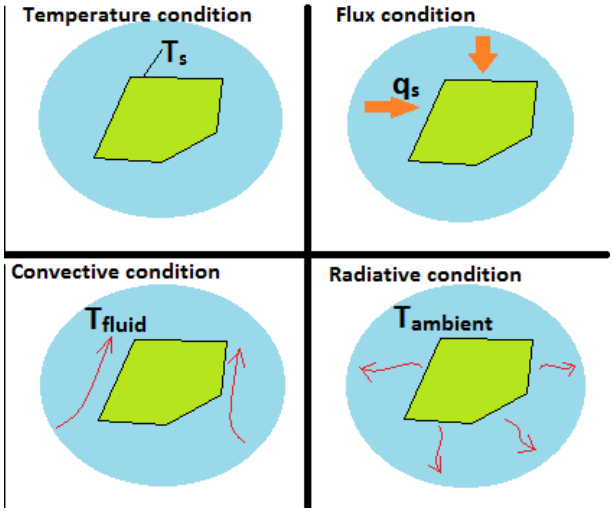

Figure 2.3: The different types of boundary conditions in heat transfer.

2.3.3. Solving the heat equation

Solving the heat equation lies at the core of thermal analysis. Therefore, it is important to know how to solve the heat equation. An exact solution of a problem can only be obtained by analytical methods. However, since analytical methods often are available for limited domains and boundary conditions, most of the time one has to use numerical methods instead. Numerical methods can give good approximations of the solution. To know if analytical solutions are available, it is important to know what some of the analytic methods are and what their limitations are.

2.4. Analytical methods to solve the heat equation

There are several ways to solve the heat equation analytically. Three analytical methods will be discussed that can be used to solve the heat equation: seperation of variables, eigenfunction expansion and the method of fundamental solution. However, it will come apparent that these methods are very limited to use in practical cases like the LPBF-processes.

2.4.1. Separation of variables

The method of separation of variables can be used only for homogeneous problem. These are problems where the boundary conditions, like the boundary flux, and the volumetric internal heat generation (or: forcing term or source) are zero. When either boundary conditions or forcing term is not zero, there is a non homogeneous problem [10]. These kinds of problems can be solved using an eigenfunction expansion or the method of fundamental solutions [10].

2.4.2. Eigenfunction expansion

When using the eigenfunction expansion, the problem is first transformed to a homogeneous problem. The solution of this transformed homogeneous problem is called the eigenfunction. This eigenfunction is used to expand the non homogeneous boundary condition and forcing term. Integration is involved in these expansion [8, 10].

2.4.3. Method of fundamental solutions

Another way to deal with non homogeneous problems is the method of fundamental solutions, also known as Green's function method [8, 10]. When using the method of fundamental solutions, the solution is obtained by using the appropriate Green's function as a kernel in a convolution integral relation, called the Green's formula. The Green's function is the impulse response of the heat equation [8, 10]:

$$\frac{\partial G(\mathbf{x},\boldsymbol{\xi},t,\tau)}{\partial t} = \alpha \frac{\partial^2 G(\mathbf{x},\boldsymbol{\xi},t,\tau)}{\partial \mathbf{x}\partial \mathbf{x}} + \delta(\mathbf{x}-\boldsymbol{\xi})\delta(t-\tau)\,, \tag{2.14}$$

where ξ and τ are a dummy variables for space and time, respectively. As one can see, the forcing term is a delta Dirac function $\delta(\mathbf{x}-\xi)\delta(t-\tau)$ that is activated at the spatial location $\mathbf{x}=\xi$ and time $t=\tau$. The boundary conditions of the Green's function are chosen such, that where the original problem has a prescribed boundary conditions, the Green's function has a homogeneous boundary condition. Also the initial condition of the Green's function is zero [10]. The solution can be calculated using the Green's formula [8, 10]:

$$T(\mathbf{x},t) = \int_0^t \int_V \frac{Q(\xi,\tau)}{c_p\rho} G(\mathbf{x},\xi,t,\tau)d\Omega(\xi)d\tau + \int_V T(\xi,0)G(\mathbf{x},\xi,t,0)d\Omega(\xi) + \\ +\alpha \int_0^t \int_S \left(G(\mathbf{x},\xi,t,\tau)\frac{\partial}{\partial\xi}T(\xi,\tau) - T(\xi,\tau)\frac{\partial}{\partial\xi}G(\mathbf{x},\xi,t,\tau)\right)\cdot \mathbf{n}(\xi)d\Gamma(\xi)d\tau \,. \tag{2.15}$$

The first term of this integral relation deals with the forcing term, the second one with the initial condition and the third integral deals with the boundary conditions. The Green's function that has to be used depends on the geometry and boundary conditions of the problem. It is not always possible to find the Green's function of a function analytically [10].

2.4.4. Limitations of analytic methods

These analytic methods are only appropriate for very simple geometries, boundary and initial conditions and forcing terms. For complex geometries and boundary conditions, the solution cannot be calculated analytically, mainly because of the complex integrals involved. This makes pure analytic methods not usable for practical problems like the thermal analysis of the LPBF-processes. Therefore, numerical methods are to be used instead to solve the heat equation [10].

2.5. Numerical methods to solve the heat equation

Numerical methods can give an approximate solution if the analytic solution cannot be found or is too complex, like is the case in LPBF. There are several methods to solve the heat equation numerically. Two type of methods will be discussed: domain methods (in specific the Finite Difference, Finite Volumes and Finite Element methods) and boundary methods (in specifically the Boundary Element Method).

2.5.1. Domain methods

Finite Difference Method (FDM) or Finite Volume Method (FVM) schemes have the advantage to have relatively simple numerical implementations for heat transfer problems. However, one of their disadvantage is that these methods are often restricted to simple geometries [11]. The Finite Element Method (FEM) is more complex than FDM and FVM, but can be more accurate and can be used for complex geometries [11]. In all these three methods the temperature field over the domain is discretized into unknowns that have to be solved [11].

2.5.2. Boundary methods

There also boundary descretization methods, like the Boundary Element Method (BEM), that only has the unknowns at the boundary [12]. By starting with the Green's formula in equation 2.15, and discretizing the integral equation in time and space, the only unknowns that have to be solved are at the boundary. After solving these unknown boundary values, the internal temperature values can be calculated by using the solved boundary values into the discretized version of the integral relation in the Green's formula. The Green's function that is used in BEM is usually the impulse response in an infinite domain [12]:

$$G(\mathbf{x}-\xi) = \frac{\exp\left(-\frac{||\mathbf{x}-\xi||^2}{4\alpha(t-\tau)}\right)}{[4\alpha\pi(t-\tau)]^{\frac{n}{2}}} \,, \tag{2.16}$$

where n is the spatial dimension.

2.5.3. Advantages and disatvantages of FDM, FVM, FEM and BEM

The advantage of FDM and FVM is that they are relatively simple, have less computation time and the matrices involved are sparse and usually symmetric [11]. However, their level of accuracy is limited and

they can mostly be applied in simple geometries. The advantage of FEM is that the matrices involved are also sparse and usually symmetric. It can also have a higher level of accuracy than FDM en FVM. The large advantage that FEM has over FDM and FVM is it can be applied to complex geometries. However its implementation is a bit more complex than FDM and FVM [11]. The BEM has the great advantage that the unknowns are only at the boundary. However it's not so accurate as FDM, FVM or FEM. Another advantage of BEM is that the matrices involved are usually not so large as FDM, FVM and FEM, but they are fully populated and not symmetric [12], which makes solving the vector-matrix equations not so efficient as is the case in sparse matrices in FDM, FVM and FEM [11]. Also the complexity of the BEM is one of the greater disadvantage of the method, since one has to find the appropriate Green's function, calculate the discretized intergrals of both the Green's function and its derivative [12]. For the mentioned reasons FEM is mostly used in thermal analysis, especially for its capability to handle complex geometries.

2.5.4. Mesh size

The physical input parameters for the numerical methods are the source, the boundary conditions and the material properties. These have an effect on the numerical mesh size and time step that have to be chosen in order to capture the behaviour of the quantity to be calculated like the temperature or flux. In the problem of this thesis, the boundary flux will be the most important input parameter. In order to capture the right behaviour of the boundary flux, the mesh along the boundary should be fine enough. If this is not the case, the behaviour of the boundary flux will not be represented good enough in the numerical solution. The steeper the boundary flux is, the finer the mesh should be. This concept is illustrated in figure 2.4, where the behaviour of a steep boundary flux is attempted to be caught in to ways: by a coarser mesh and by a finer mesh. It is very clear that the finer mesh catches the boundary flux behaviour better than a coarser mesh. If the boundary flux is however not steep, but smooth, a coarser mesh can be used, as is illustrated in figure 2.5.

In LPBF the laser causes very high temperature gradient near the laser spot [2, 3]. This laser is often modelled as the source term in the numerical methods. Because the temperature is very steep near the laser spot, a very fine mesh around the laser spot is required. This makes the numerical calculation very inefficient [11]. There is however a computationally efficient way to do the thermal analysis in LPBF-processes by decouple the laser modelling from the numerical method in a certain way. This is called the semi-analytic method and will be discussed next.

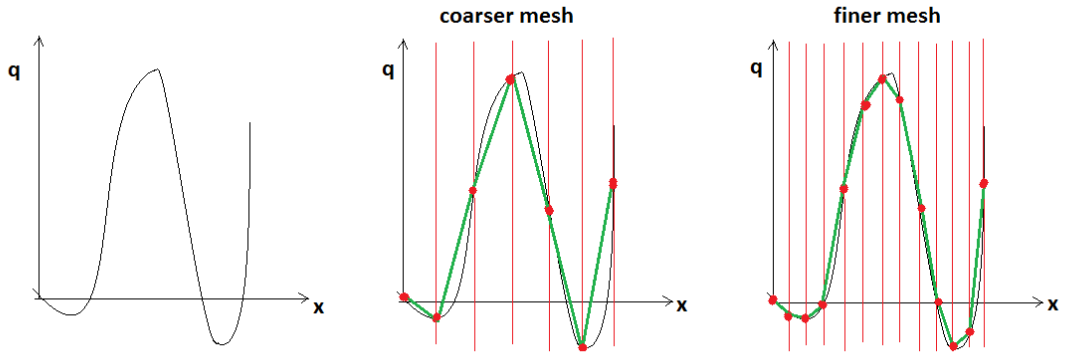

Figure 2.4: On the left is a steep boundary flux that has to be represented in the numerical solution. The middle and right figures show in green the numerical discretization of the original boundary flux. The red dots are the sampling points at which the boundary flux is taken. The horizontal distance between the points is the mesh size. The middle figure uses a coarser mesh size, while the right figure uses a fine mesh size.

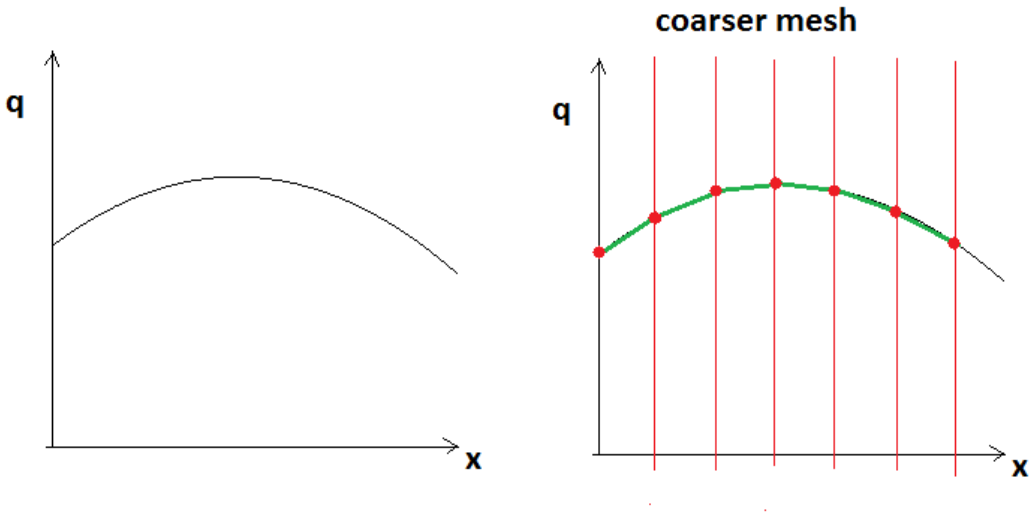

Figure 2.5: On the left is a smooth boundary flux that has to be represented in the numerical solution. The right figure shows in green the numerical discretization of the original boundary flux. The red dots are the sampling points at which the boundary flux is taken. The horizontal distance between the points is the mesh size. For this smooth boundary flux a coarser mesh can be used.

2.6. Semi-analytic method

Numerical methods are necessary in modeling the thermal behaviour of LPBF-processes, but for purely numerical methods a very fine mesh is required to model the laser, since near the laser spot the temperature rises immensely within a radius that has a scale that is much smaller compared to scale of the domain. Because large amount of heat is concentrated on a small spot, very high temperature gradients near the laser spot arise. This causes computational inefficiency, since a fine mesh is required to capture the behaviour of these steep gradients. However, there is an alternative for purely numerical modelling called the semi-analytic method [2, 3] that can resolve the problem of the requirement of a fine mesh. The general idea of this method will be discussed next.

2.6.1. General idea of the semi-analytic method

The semi analytic method offers a way to decouple the modelling of the laser from the numerical problem, by letting an analytic solution deal with the modelling of the laser instead [2, 3]. This analytical solution is usually a known solution of a point source in an infinite or semi-infinite domain. Because this analytic solution is for infinite or semi-infinite space, it does not take the boundary conditions into account. Therefore a numerical field is introduced to correct for the boundary conditions, by taking the negative value of the flux of the analytic solution at the boundary locations as an input. Then a superposition of the analytical field and numerical field is done. When the boundary conditions of the analytic solution and numerical solution are added up, the produce a zero flux boundary condition, which is required for LPBF models. In figure 2.6 one can see a visualization of the general concept. Now the general idea of the semi-analytic method is known, it is important to know how the semi-analytic method is applied in the thermal modelling of LPBF-processes. This will be discussed next.

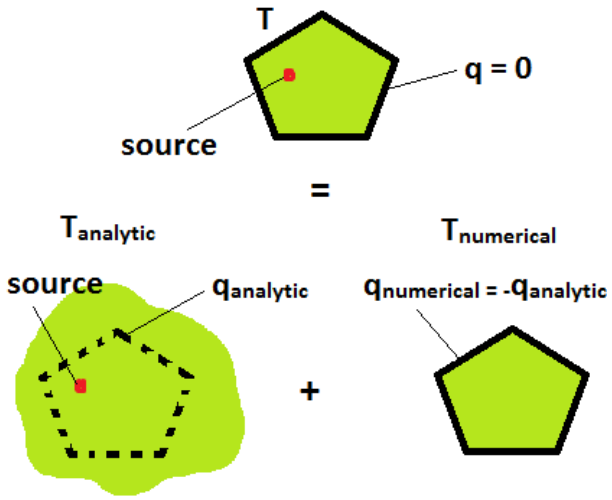

Figure 2.6: The temperature for the superposition of an analytic solution in infinite domain and a numerical solution that corrects for the boundary conditions. The numerical correction is done by taking the negative value of the flux of the analytic solution at the boundary as an input.

2.6.2. Application of the semi-analytic method in LPBF-processes

In the thermal modelling of the LPBF-proces, the semi-analytic method uses the analytic solution of the heat equation for a point sources in infinite space. It is important to gain insight about the analytic solution, since its temperature and flux values at the boundary are the input for the numerical correction field.

In LPBF the laser scan is a continuous line, but can be modelled by discretizing it into multiple point sources [2] that are added up, as will be explained in detail in the next chapter. Therefore, having insight in how the semi-analytic method works for a single point source, will give insight in how it works for a laser scan. Suppose that within an infinite domain there is a point source that has a heat power intensity Q and is activated at a position $\mathbf{x_s}$ and on time t_0. Then based on [8, 10, 12] the temperature field for n-dimensions is:

$$T^{\text{analytic}}(\mathbf{x}, t) = \frac{Q}{c_p \rho} \frac{\exp\left(-\frac{||\mathbf{x}-\mathbf{x_s}||^2}{4\alpha(t-t_0)}\right)}{(4\pi\alpha(t-t_0))^{\frac{n}{2}}} . \tag{2.17}$$

As one can see, the exponent contains an argument that depends on the distance between the source point position $\mathbf{x_s}$ and the field point position $\mathbf{x}$. One can also see that the temperature depends on the passed time $t - t_0$. The temperature has a maximum value at the source point location. When time passes, the temperature gets more distributed over time [8].

After knowing how the analytic field looks like, it is possible to determine the boundary conditions for the numerical field. The numerical field has boundary conditions that are related to the analytic field. Based on [2, 3] the boundary conditions of the numerical field are as follows:

$$\begin{aligned} T^{\text{numerical}}(\mathbf{x}, t) &= T_{S_1} - T^{\text{analytic}}(\mathbf{x}, t) && \text{for } \mathbf{x} \in S_1 \\ \mathbf{n} \cdot \nabla T^{\text{numerical}}(\mathbf{x}, t) &= -\mathbf{n} \cdot \nabla T^{\text{analytic}}(\mathbf{x}, t) && \text{for } \mathbf{x} \in S_2 . \end{aligned}$$

Where S_1 is the part of the boundary where the desired temperature boundary conditions T_{S_1} are prescribed, and S_2 is the part of the boundary where the desired zero flux boundary conditions are prescribed. As long as the source is not close to the boundary, the fluxes that have to be corrected at S_2 are smooth enough and thus can be captured by a coarse mesh in the numerical solution. However, when the point source is close to the boundary, the boundary flux loses its smoothness, as will be explained next. In LPBF-processes the source is always close to the boundary.

2.6.3. Semi-analytic method when the laser is close to the boundary

The analytic solution for a single source has high gradients near the source point. By dealing with the point source analytically, the numerical field does not require a fine mesh to capture the high gradient,

as long as the laser is far away from the boundary. However, when the laser is close to the boundary the gradients that need to be corrected become steeper, as can be seen in figures 2.7. It can be seen that when the point source is close to the boundary, the temperature shows steeper gradients along the boundary. This requires a finer mesh for the numerical correction field [2, 3]. Thus, the advantage of the semi-analytic solution the using a coarse mesh in the semi-analytic method is lost. However, it is possible to have an analytic solution with a smoother boundary flux, as will be discussed soon. But first, what does it mean when the point source is 'close enough'?

The distance that determines if the point source is close to the boundary, when using the semi-analytic method, is called the critical distance H_c. The critical distance is the distance of the laser point to the boundary, where the high flux gives a numerical temperature field with the maximum allowable error. The critical distance is studied by [2] for a 1D domain, as can be seen in figure 2.8. How the critical distance in figure 2.8 relates to the numerical error and mesh size is illustrated in figure 2.9. In the next chapter, H_c will be specified. Now it is known that the source point is close to the boundary if it at the critical distance or closer the boundary, one can look at how the high gradients are dealt with using the method of (equidistant) imaging for planar boundaries. Circular boundaries will be discussed afterwards.

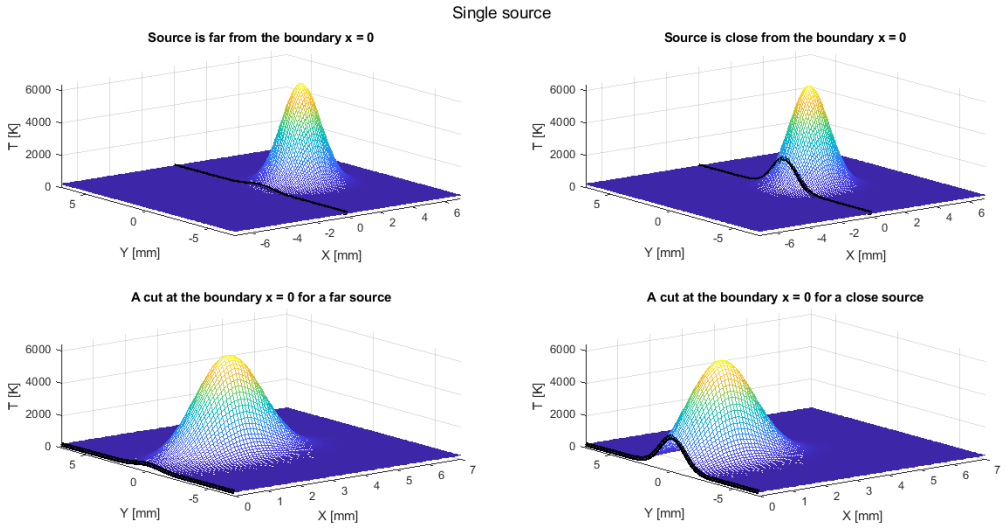

Figure 2.7: Temperature of a single source in a 3D infinite space, at the plane $z = 0$. The left plots are for sources far from the original domain boundary $y = 0$, and the right plots are close to it. The lower plots are cut of at the boundary so that the temperature contour along the boundary (the black thick line) can be seen.

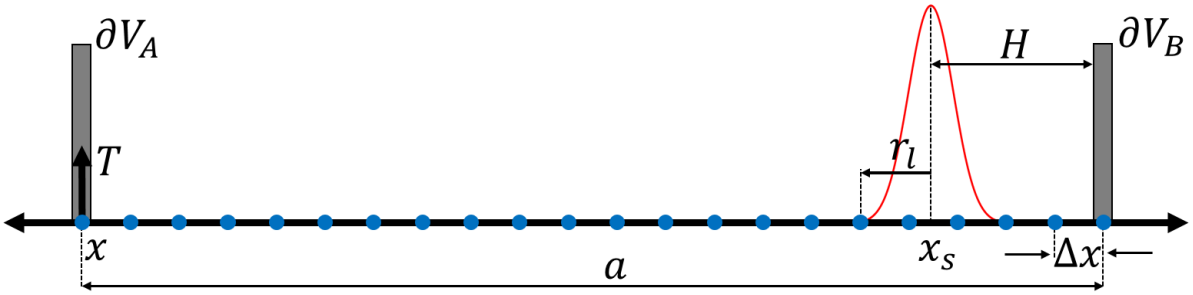

Figure 2.8: Note: Reprinted from "Thermal modelling of Selective Laser Melting: a semi-analytic approach", by M.F. Knol, 2016. This is a schematic illustration of a single source in a 1D domain that is bounded by the two boundaries ∂V_A and ∂V_B. The source is a distance H apart from the boundary, and the boundaries are a distance $a = 40$ mm apart. The spot radius r_l is 35 μm. The source energy is 5000 J and the material parameters are: $k = 40.5$ W/(mK), $c_p = 963$ J/(kgK) and $\rho = 4420$ kg/m^3.

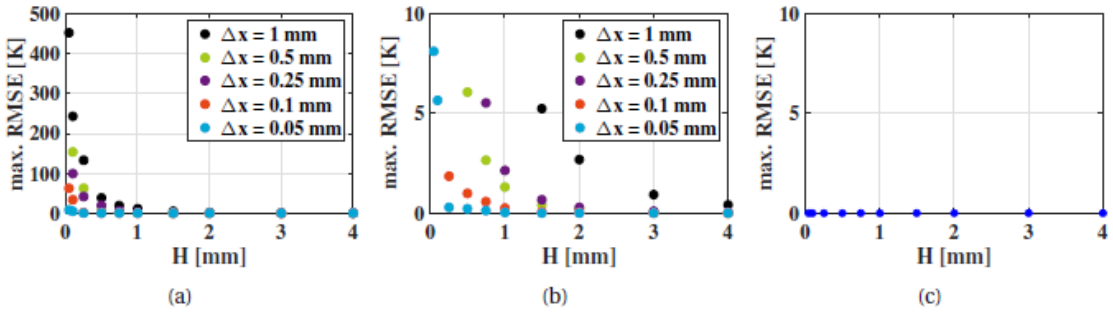

Figure 2.9: Note: Reprinted from "Thermal modelling of Selective Laser Melting: a semi-analytic approach", by M.F. Knol, 2016 [2]. The maximum value of the root-mean-square error (RMSE) for different distances of the laser source to the boundary H in the situation sketched in figure 2.8. In (a) the boundary conditions are enforced using standard finite differences with different grid sizes Δx. In (b) we see a close-up of (a). In (c) the boundary conditions are enforced by using the method of images (equidistant).'

2.7. The method of images for planar boundaries

The method of images resolves the problem of having high gradients close to planar boundaries [2, 3]. This method is used in solving the heat equation for a point source in a semi-infinite domain [8, 10, 12]. This solution can have either a zero temperature or a zero flux boundary condition [8, 10, 12]. For the problem in this thesis a zero flux boundary condition is needed. The idea of the method of imaging in the semi-analytic method is that for the analytic solution an image source is placed outside the domain boundary at a distance equal to the distance between the source inside the domain and the boundary. This is why it will be called 'equidistant imaging' in this thesis. This idea is illustrated in figure 2.10. One can see a comparison of the situation where no imaging is used and when imaging is used. The two top figures show the temperatures in infinite space. As one can see at the right plot, an additional source, the image source, is added outside the boundary. The bottom figures show that the boundary flux has steep gradients when no imaging is applied, but is zero when equidistant imaging is applied.

How does the analytic solution look if the method of images is used? If the source is located at coordinates $(x_s, 0, 0)$ and the boundary is at $x = 0$, then according to [8, 10] for zero flux boundary conditions the solution looks as follows::

$$T^{\text{analytic}}(x,y,z,t) = \frac{Q}{c_p\rho}\left(\frac{\exp\left(-\frac{(x-x_s)^2+y^2+z^2}{4\alpha(t-t_0)}\right)}{(4\pi\alpha(t-t_0))^{\frac{3}{2}}} + \frac{\exp\left(-\frac{(x+x_s)^2+y^2+z^2}{4\alpha(t-t_0)}\right)}{(4\pi\alpha(t-t_0))^{\frac{3}{2}}}\right). \tag{2.18}$$

This solution is a superposition of two terms. The first term will be called the source term and the second term the image term. In the next chapter, it will be relevant to also know the solution when there is zero temperature boundary condition. According to [8, 10] the solution for zero temperature at the boundary looks as follow:

$$T^{\text{analytic}}(x,y,z,t) = \frac{Q}{c_p\rho}\left(\frac{\exp\left(-\frac{(x-x_s)^2+y^2+z^2}{4\alpha(t-t_0)}\right)}{(4\pi\alpha(t-t_0))^{\frac{3}{2}}} - \frac{\exp\left(-\frac{(x+x_s)^2+y^2+z^2}{4\alpha(t-t_0)}\right)}{(4\pi\alpha(t-t_0))^{\frac{3}{2}}}\right). \tag{2.19}$$

As can be seen, for a zero flux condition we have a + sign before the image term instead of a − sign.

The method of equidistant imaging works fine for planar boundaries, since the zero flux conditions are satisfied exactly along the whole boundary. However, for circular boundaries, it is difficult or even impossible to use the method of imaging to realise a zero flux along the whole circular boundary. If one attempts to use the method of images, the flux is in general not zero along the boundary. This is illustrated in figure 2.11. One can see that the contours for both the cases of no images and images are not perpendicular to the circle. This means that the boundary flux is not zero. An analytic solution could be sought that fulfills the zero flux condition at circles, but it will be too complex, since eigenfunction

expensions for three dimension have to be done [10]. Moreover, a coordinate transformation from Cartersian coordinates to cylindrical coordinates has to be made. This will lead to having different Bessel functions in the eigenfunction expansion, that require calculating the zero's of multiple Bessel functions. If this approach would be taken the computational cost would eventually rise. Instead of the exact zero flux condition solution, an attempt has been made to smoothen the boundary flux of equidistant imaging at circular boundaries my means of a modulation. This will be discussed next.

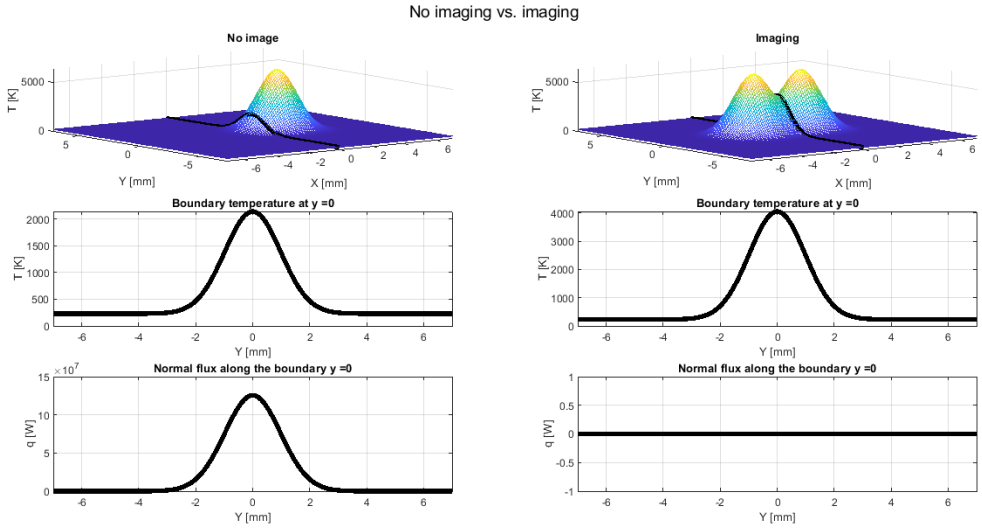

Figure 2.10: The source is applied on the positive side of x-axis, and the boundary is the line $x = 0$. In the left plots no imaging is applied, and in the right plots imaging is applied. The two top plots show temperature of the single source in infinite space, at the plane $z = 0$. The black line are the contours of the temperature along the boundary. The two plots below them the boundary temperature at the boundary $x = 0$ are shown. The lower plots are the boundary fluxes along the boundary.

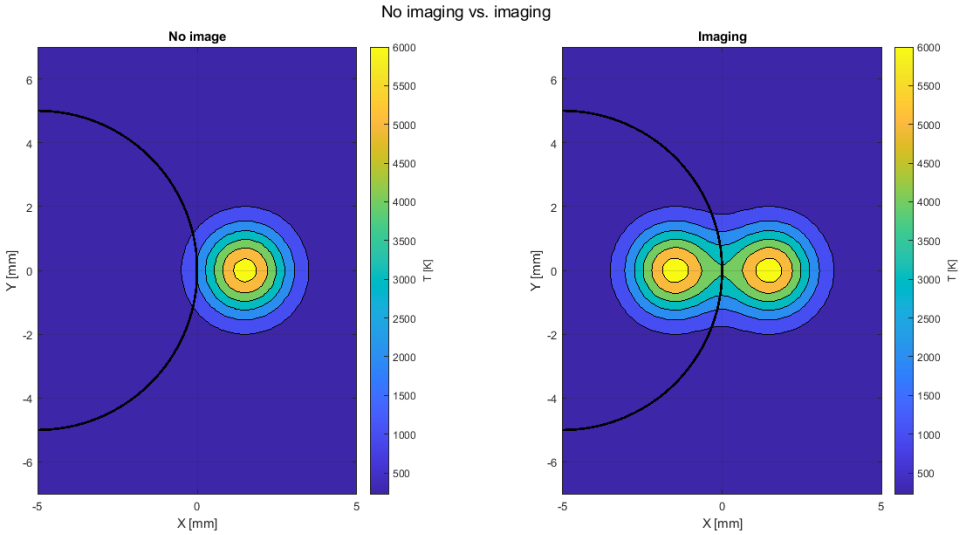

Figure 2.11: Contour plots of the temperature, where a source is applied outside the circle. In the left plots no imaging is applied, and in the right plots imaging is applied. The black circle is the circular boundary.

2.8. Method of images for circular boundaries

The method of images gives exactly a zero flux condition for planar boundaries. However if there is a circular boundary and the original source and image source are placed equidistant to the boundary, the

zero flux condition does not apply at the whole circular boundary. The fluxes could still be too steep for the semi-analytic method, and a fine mesh would be required for the numerical correction field. An attempt has been made by [4] to approach a zero flux boundary for a moving laser by using modulation factor to scale the image term. If the laser is discretized into multiple source points, then based on [4] the modulation factor f_d is:

$$f_d = \frac{v_i}{v_s}, \tag{2.20}$$

where v_s is the velocity of the laser, and v_i is the velocity of the laser scan that is formed by the image sources. It was shown by [4] that this modulation gave good results and smoothens the flux along the boundary.

However, if it is possible to obtain a smoother flux than is done by modulation, it would be possible to use a more coarser mesh in the semi-analytic method. Therefore, it would be interesting to investigate how in other fields outside heat conduction is dealt with solving partial differential equations for domains with circular boundaries. Perhaps that other fields could give an option or suggestion that would be practical for thermal analysis for domains with circular boundaries. In electrostatics circular boundaries are very common. Therefore, an investigation of the solutions in electrostatics will be made.

2.9. Method of images in electrostatics for domains with circular boundaries

The method of imaging for planar boundaries is used in the field of electrostatics, in the exact same way it is used in thermal analysis [12]. For circular boundaries however, there is a simple analytic solution in electrostatics, contrary to thermal analysis. In electrostatics however, a different imaging method than equidistant imaging is used for circular boundaries: inverse imaging. In this thesis, an attempt will be made to construct an analytic expression for thermal analysis circular boundaries, inspired by the solution of electrostatics with circular boundaries, where inverse imaging is used. But first, it is important to have an idea of the electrostatics problem.

2.9.1. The electrostatics problem

The field quantity that occurs in electrostatics is the electric potential ϕ. In the electrostatic problem, that is interesting for this thesis, a point charge is placed outside an infinitely long cylinder with zero potential at the cylinder [13, 14], as can be seen in figure 2.12.
The governing equation of this problem is:

$$\nabla^2\phi = -C\delta(\mathbf{x} - \mathbf{x_s}) \in \Omega\,. \tag{2.21}$$

Here C is a constant that is a product of certain electrical material properties, which are irrelevant for this thesis to specify. The point source is represented by a Delta Dirac function $\delta(\mathbf{x} - \mathbf{x_s})$ that is activated at the location $\mathbf{x} = \mathbf{x_s}$. The boundary condition on the circular boundary that has a radius R is:

$$\phi = 0\,. \tag{2.22}$$

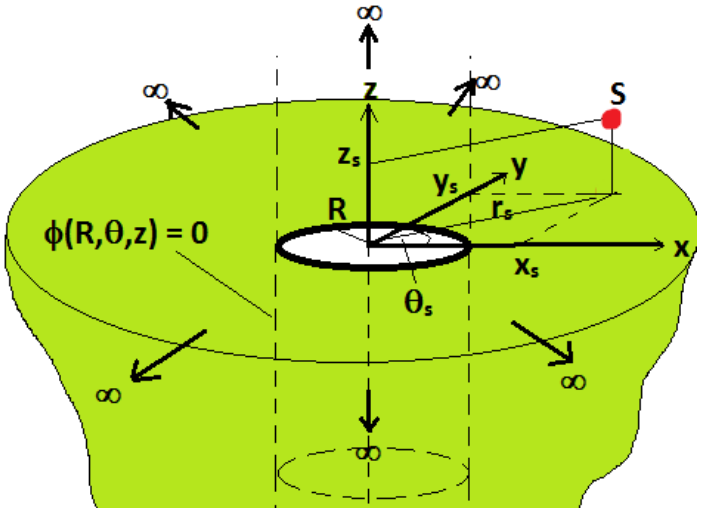

Figure 2.12: The plane at $z = 0$ in an infinite domain with a infinitely long cylindrical cavity of radius R. At the cylinder the electrical potential ϕ is zero. The point source S is located at Cartesian coordinates (x_s, y_s, z_s) and polar coordinates (r_s, θ_s, z_s).

2.9.2. Inverse imaging

If there would be a planar boundary the solution in electrostatics would use equidistant imaging, just like thermal analysis [13, 14, 12]. However in case of a circular boundary the image source in electrostatics is not equidistant to the boundary, but at the inverse point with respect to the radius of the circle [13, 14, 12]. This will be referred to in this thesis as 'inverse imaging'.

The way the inverse point is determined in polar coordinates is as follows. Suppose that the cylinder has a radius R and the source point has a radius r_s. If inverse image is located at the inverse point of the source with respect to the circle, then the radius of the image point r_i is given by:

$$r_i = \frac{R^2}{r_s}\,. \tag{2.23}$$

The radius of the source term and image term have an inverse relation [12]. Therefore we call this type of imaging: inverse imaging. Both the source and the image are at an angle θ_s [10, 12].

2.9.3. The solution

Knowing how the inverse point is determined, it is possible to construction of the solution in electrostatics using the method of inverse imaging. This will be done in steps. First one has to know the infinite solution of the electric potential ϕ in electrostatics for a single point charge in an infinite domain without a circular cavity. According to [10, 12, 13, 14] this has the following form:

$$\begin{aligned}\phi &= -\frac{C}{4\pi||\mathbf{x}-\mathbf{x_s}||} \\ &= \frac{C}{4\pi\sqrt{(r^2+r_s^2-2rr_s\cos(\theta-\theta_s)+(z-z_s)^2)}}\,.\end{aligned} \tag{2.24}$$

The point source is located at $\mathbf{x_s}$ with polar coordinates (r_s, θ_s, z_s).

However for a domain with a circular cavity, an additional image term should be added in order to have a zero potential at the cylinder. This results in the second step: adding the inverse image term. The solution then becomes:

$$\phi(r,\theta,z) = \frac{C}{4\pi\sqrt{r^2+r_s^2-2rr_s\cos(\theta-\theta_s)+(z-z_s)^2}} - \frac{C}{4\pi\sqrt{\gamma(r^2+r_i^2-2rr_i\cos(\theta-\theta_s))+(z-z_s)^2}}\,, \tag{2.25}$$

where γ is a geometrical scaling factor that is defined as:

$$\gamma = \frac{r_s}{r_i} \,. \tag{2.26}$$

The factor γ gives a relation between r_s and r_i. It is also to relate the boundary radius R and the laser radius r_s. Equations 2.23 and 2.26 give us a relation between laser radius, the boundary radius and gamma:

$$\gamma = \frac{r_s^2}{R^2} \,. \tag{2.27}$$

Thus the factor γ allows this special relation between the boundary radius and the laser radius.

In equation 2.25 the image term has not only a different location of the image point than equidistant imaging, but also the factor γ is involved. This factor is important to ensure the zero potential at the boundary radius, as shall be shown now. Using both the expressions of γ in equations 2.26 and 2.27 in equation 2.25 for $r = R$, one gets the following results:

$$\begin{aligned}
\phi(R,\theta,z) &= \frac{C}{4\pi\sqrt{R^2 + r_s^2 - 2Rr_s\cos(\theta-\theta_s) + (z-z_s)^2}} - \frac{C}{4\pi\sqrt{\gamma(R^2 + r_i^2 - 2Rr_i\cos(\theta-\theta_s)) + (z-z_s)^2}} \\
&= \frac{C}{4\pi\sqrt{R^2 + r_s^2 - 2Rr_s\cos(\theta-\theta_s) + (z-z_s)^2}} - \frac{C}{4\pi\sqrt{\gamma R^2 + \gamma r_i^2 - 2R\gamma r_i\cos(\theta-\theta_s) + (z-z_s)^2}} \\
&= \frac{C}{4\pi\sqrt{R^2 + r_s^2 - 2Rr_s\cos(\theta-\theta_s) + (z-z_s)^2}} - \frac{C}{4\pi\sqrt{r_s^2 + \gamma\frac{r_s^2}{\gamma^2} - 2Rr_s\cos(\theta-\theta_s) + (z-z_s)^2}} \\
&= \frac{C}{4\pi\sqrt{R^2 + r_s^2 - 2Rr_s\cos(\theta-\theta_s) + (z-z_s)^2}} - \frac{C}{4\pi\sqrt{r_s^2 + \frac{r_s^2}{\gamma} - 2Rr_s\cos(\theta-\theta_s) + (z-z_s)^2}} \\
&= \frac{C}{4\pi\sqrt{R^2 + r_s^2 - 2Rr_s\cos(\theta-\theta_s) + (z-z_s)^2}} - \frac{C}{4\pi\sqrt{r_s^2 + R^2 - 2Rr_s\cos(\theta-\theta_s) + (z-z_s)^2}} \\
&= 0 \,.
\end{aligned}$$

As one can see, the zero potential is ensured by means of using the inverse point as an image point and using the factor γ.

2.10. Similarities and dissimilarities between electrostatics and heat conduction problem

In thermal analysis inverse imaging for circular boundaries in not used. However one could question if inverse imaging would be applied for thermal analysis, would it give a boundary flux that is smooth enough to be use in the semi-analytic method. The idea of using inverse imaging in heat conduction is inspired by the similarities between the heat conduction problem of this thesis and the electrostatic problem for circular boundaries. These similarities are: the geometrical shape of the boundaries, the presence of the differential operator Laplacian ∇^2 in both the Lapace's equation (for electrostatics) and the heat equation, and the fact that for planar boundaries both problems use the same imaging method, namely equidistant imaging. The last similarity could suggest that if electrostatics and heat conduction both use equidistant imaging for planar boundary, and electrostatics uses inverse imaging for circular boundaries, it could be possible that inverse imaging could also be used in heat conduction in the case of circular boundaries.

However, it is important to look at the dissimilarities between the electrostatic problem and the heat transfer problem, that could cause different results. The dissimilarities between the electrostatic problem and the heat transfer problem of this thesis is not only a dissimilarity in the type of governing equation (i.e. Laplace's equation for electrostatics and heat equation for heat conduction), but also the

type of field quantity to be calculated. In the heat conduction problem the interest is namely on the gradient of the temperature field, not the temperature field itself. While the electrostatic solution does not ensure a certain the boundary gradient, but only ensures a zero electric potential. Nevertheless, it is worth the effort to investigate inverse imaging for the heat conduction problem in this thesis, based on the similarities. Because even if the inverse imaging does not give a zero heat flux at the boundary, it still may be a useful imaging method if it can give a smooth boundary flux along the boundary. After all, having an exact zero heat flux at the boundary is not our specific interest, but rather obtaining a boundary flux that is smoother than the one obtained from modulation. The methodology how this will be investigated will be explained in the next chapter.

3

Methodology

In chapter 1 the thesis question was formulated as: 'How appropriate is inverse imaging method in the semi-analytic thermal modelling of LPBF-processes for cylindrical boundaries compared to modulated equidistant imaging method?' In this chapter the methodology for answer the thesis question will be explained. In general the answer will be given by investigating how the smooth the boundary flux along the boundary of the inverse imaging is.

First, an illustration of the geometrical domains of interest, the boundary conditions and the location of the inverse images will be given. Next, the construction of the temperature profile that makes use of inverse imaging, inspired by equation 2.25, will be derived. Firstly by explaining how the laser scan is approximated by an appropriate discretization of point sources, and then showing the expression of the temperature that uses inverse imaging method for a single source. The expression will be used to add multiple sources together in order to form a scanning pattern. After the temperature profile is known, the boundary flux can be derived from it. The expression of the boundary flux will be shown at the end of this chapter. The smoothness of the boundary flux for inverse imaging will be further analyzed in the next chapter.

3.1. Geometry of the domain and boundary conditions

As explained earlier, a new imaging method will be analyzed in order to find a smooth enough analytic solution for cylindrical boundaries. In this thesis the geometry that will be considered is the boundary of with quart circular shape, for both concave and convex boundary types.

3.1.1. Concave and convex domains

Concave domains in this thesis are defined by domains that have a circular boundary, and where the laser scans the domain outside the radius of the circular boundary. Convex domains also have a circular boundary, but the laser scans the domain inside the radius of the circular boundary. An impression of these domains can be seen in figure 3.1.

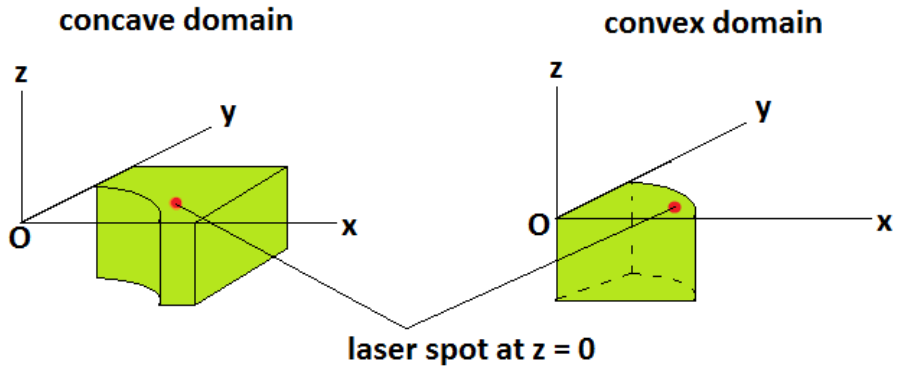

Figure 3.1: The domains of interest contain a quarter cylindrical boundary, one domain is concave, while the other is convex.

3.1.2. Boundary conditions

After knowing how the domain looks like, the boundary conditions on the circular boundaries can be explained. Using the concave domain in figure 3.2 as an example (the same applies for convex boundaries) the boundary conditions that apply to the eventual semi-analytic solution can be formulated as follows [3]:

- The top plane $z = 0$ is adiabatic, i.e. the normal flux to the plane q_{top} should be zero.
- The bottom plane has a constant temperature $T_{\text{base}} = 230$ K.
- The remaining sides of the domain are adiabatic, i.e., the normal flux to the sides q_{side} is zero.

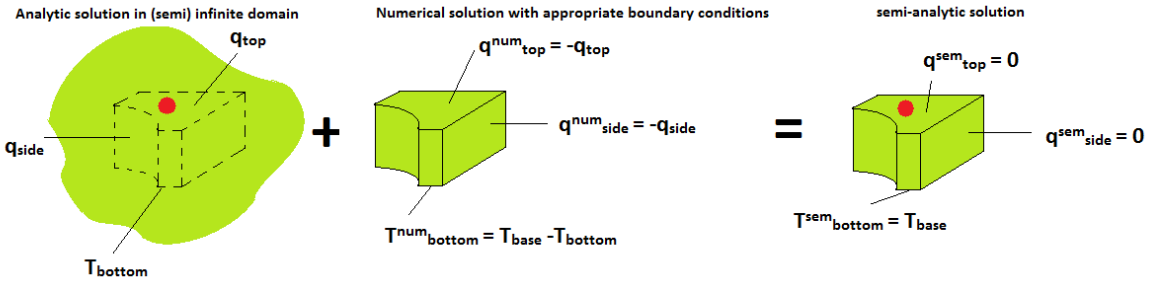

Figure 3.2: Schematic illustration of the semi-analytic method with the desired boundary condition. This is a concave domain.

3.1.3. The location of the sources and their images

After discussing the geometrical settings and defining the boundary conditions, it is important to know where the sources are applied and how the locations of their images relate to the location the sources. To determine these locations, the radius of the boundary will be denoted as R, and chosen to be 1 mm, which is in a scale that is common in LBPF [3].

The radius from the origin of the circle to the laser spot will be denoted as r_s. In figure 3.3 one can see an illustration of the plane $z = 0$ when a single source is applied, without image sources. An illustration of the case where an image is introduced is given in figure 3.4. As can be seen, the image has a radius r_i and is always outside the boundary. It is also clear from the figures that the angle of both the source and its image have the same value θ_s, as will be discussed later in this chapter.

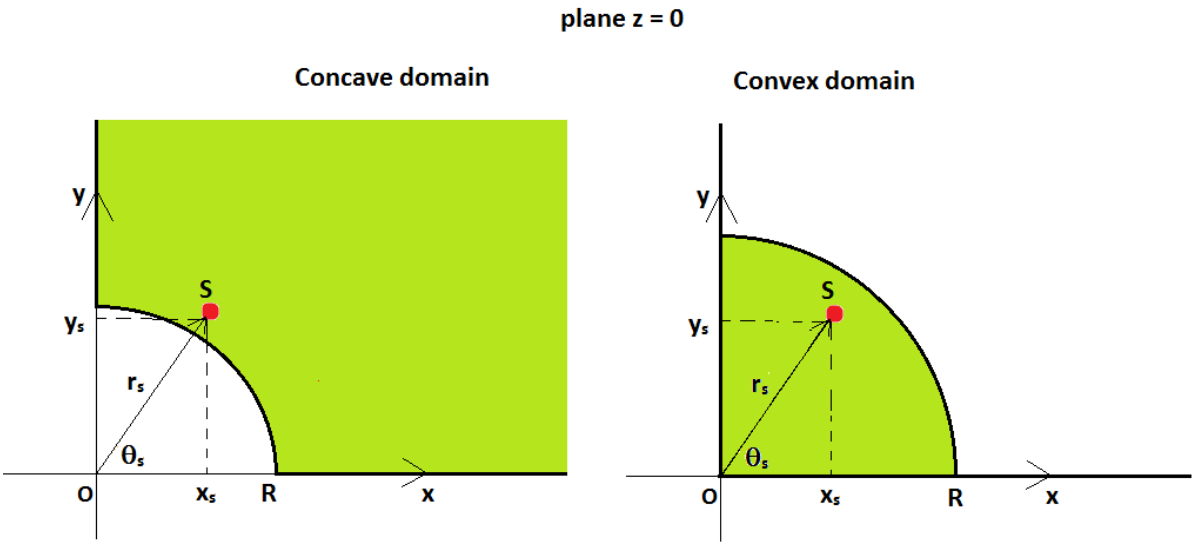

Figure 3.3: An illustration of the plane $z = 0$ for a single source. The cylindrical boundary has a radius R. A single point source is placed at point s, with Cartesian coordinates $(x_s, y_s, 0)$ and cylindrical coordinates $(r_s, \theta_s, 0)$.

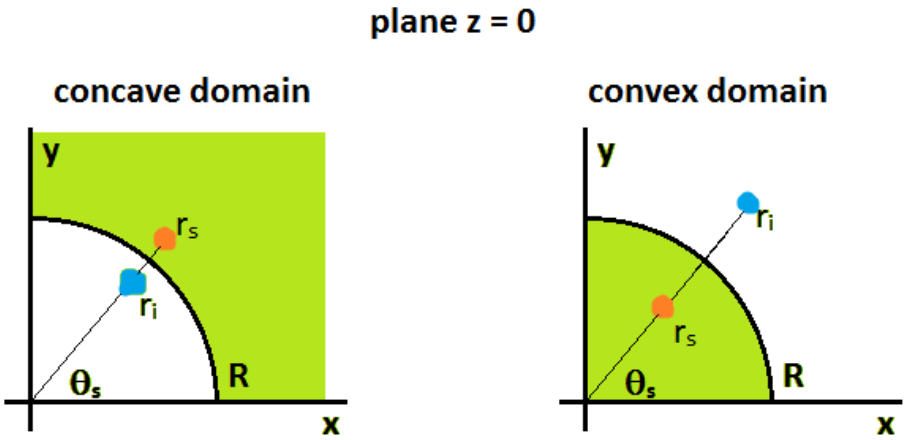

Figure 3.4: An illustration of the plane $z = 0$ for a single source s with its image source i. The original source has a radius r_s, while the image source has a radius r_i. Both sources have the same angles θ_s.

The radius to the laser will be located at the critical distance H_c to the boundary, since this distance gives rise to more numerical error due to fineness of the mesh as was explained in chapter 2. Figure 2.9 will be used to choose an appropriate critical distance for a mesh size of $\Delta x = 0.05$ mm. If critical distance of $H_c = 0.1$ mm is chosen, an error of 6 K will be given, which is a reasonable numerical error.

If the laser radius is at the critical distance, then the laser radius r_s should be equal to $r_s = R + H_c$ for a concave boundary, and $r_s = R - H_c$ for a convex boundary. Knowing the radius of the source, one can calculate the image radius for equidistant imaging r_e as follows:

$$\begin{aligned} r_e &= R \pm |R - r_s| \\ &= 2R - r_s \ . \end{aligned} \tag{3.1}$$

The radius of an inverse image point was defined in equation 2.23. The inverse image point is therefore

located at the radius r_{inv}:

$$r_{\text{inv}} = \frac{R^2}{r_s} \,. \tag{3.2}$$

Based on the mentioned parameters and definitions, the values of R, r_s, H_c, r_e and r_{inv} are calculated and shown in table 3.1, for both concave and convex boundaries.

To illustrate how r_e and r_{inv} change with r_s the graphs of the image position of both imaging methods are plotted as a function of the laser scan position in figure 3.5. This figure shows nicely how r_s and r_e are related linearly, and how r_s and r_{inv} show an inverse relation. It also shows that r_e and r_{inv} at the critical distances are almost identical. One may think that the imaging methods should also have similar fluxes. This reasoning is however not correct, because the inverse imaging does not only introduce a (slightly) different imaging location, but also a new scaling factor γ, as is applied in equation 2.25 for electrostatics, and as will be shown later in chapter. The impact of this factor may play a role in the smoothness of the boundary flux.

R	H_c	r_s (concave)	r_s (convex)	r_e (concave)	r_e (convex)	r_{inv} (concave)	r_{inv} (convex)
1 mm	0.10 mm	1.10 mm	0.90 mm	0.90 mm	1.10 mm	0.91 mm	1.11 mm

Table 3.1: Geometric parameters.

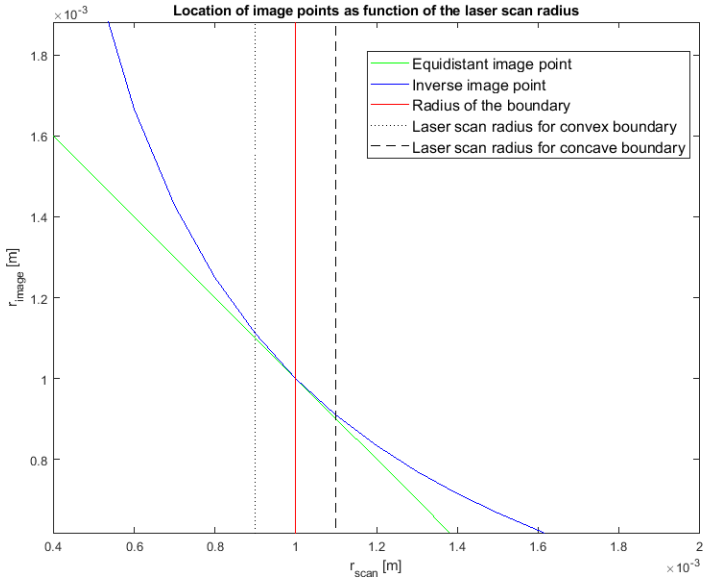

Figure 3.5: The position of the inverse point (vertical axis) as a function of the position of the laser scan (horizontal axis), in the case of the chosen boundary radius $R = 1$ mm and critical distance $H_c = 0.1$ mm. The green curve represents the positions of the image points for equidistant imaging. The blue curve presents the positions of the image points for inverse imaging expressed in equation 2.23. The black lines are the chosen laser scan radii r_s mentioned in table 3.1 for both concave and convex boundaries. The red line is the boundary radius $R = 1$ mm. The intersection of the black lines with the green curve gives at the vertical axis the positions of the equidistant image positions for concave and convex boundaries. The intersection of the black lines with the blue curve gives at the vertical axis the positions of the inverse image positions for concave and convex boundaries.

3.2. The temperature profile for inverse imaging with a single source

After having a clear vision of the geometrical parameters, the temperature profile for inverse imaging will be constructed now for a single source. Multiple sources will be discussed later.

The aim is to construct a thermal image term that is similar to the image term in electrostatics in two geometrical aspect:the inverse point as image point and the factor γ. As can be seen in equation

2.25, the distance in the image term is multiplied by γ. Therefore the temperature profile that will be constructed for inverse imaging has the following expression for a single source:

$$T(x,y,z,t) = \frac{Q}{c_p\rho}\left(\frac{\exp\left(-\frac{r^2+r_s^2-2rr_s\sin(\theta-\theta_s)+(z-z_s)^2}{4\alpha(t-t_0)}\right)}{(4\pi\alpha(t-t_0))^{\frac{3}{2}}} + \frac{\exp\left(-\frac{\gamma(r^2+r_{\text{inv}}^2-2rr_{\text{inv}}\sin(\theta-\theta_s))+(z-z_s)^2}{4\alpha(t-t_0)}\right)}{(4\pi\alpha(t-t_0))^{\frac{3}{2}}}\right) \tag{3.3}$$

Contrary to the image term for electrostatics in equation 2.25, in this equation the image term has a plus sign before it, instead of a minus sign. This is similar to planar boundaries: in equidistant imaging for planar boundaries a minus sign before the image term is placed if the boundary conditions prescribe zero temperature, but a plus sign before the image term is used, if the boundary conditions prescribe a zero boundary flux. This is also the case for electrostatic problems with equidistant imaging for planar boundaries: a minus sign before the image term for zero potential, and a plus sign before the image term for zero normal gradients. Based on the temperature profile for a single source, one can construct a temperature profile for a laser scan that is discretized into multiple sources. But first, one has to know the correct process parameter in order to do a proper discretization of the laser scan.

3.3. Modelling the laser scan & process parameters

The laser scan in this thesis will be a circular arc near the boundary. It is not convenient to model the laser as a continuous source, as shall be shown. Therefore, an appropriate approximation of the source will be done by discretizing the laser scan into multiple point sources with specific distances and time steps and certain power intensities.

3.3.1. Governing equation

The laser scan is represented in the heat equation by the source term. Properties of the laser scan are: the scanning velocity $\mathbf{v_s}$ that has a magnitude v_s, the heat generation per meter P and the absorbtivity A. Based on [8], the governing equation of a laser scan can be modelled as:

$$\frac{\partial T}{\partial t} = \alpha\nabla^2 T + \frac{AP}{\rho c_p}\delta(\mathbf{x} - \mathbf{v_s}(t-t_0) - \mathbf{x_0})\,. \tag{3.4}$$

As can be seen, the source is modelled as a delta Dirac function $\delta(\mathbf{x} - \mathbf{v_s}(t-t_0) - \mathbf{x_0})$ that is activated at starting position $\mathbf{x_0}$ and beginning time t_0. In order to find the analytic solution in infinite domain, Green's formula [8, 10] in equation 2.15 can be used:

$$\begin{aligned} T^{\text{analytic}}(\mathbf{x},t) = &\int_0^t\int_0^\infty\int_0^\infty\int_0^\infty \frac{\exp\left(-\frac{||\xi-\mathbf{x}||^2}{4\alpha(\tau-t)}\right)}{(4\pi\alpha(\tau-t))^{\frac{3}{2}}}\frac{AP}{\rho c_p}\delta(\boldsymbol{\xi} - \mathbf{v_s}(\tau-t_0) - \mathbf{x_0})d\xi_1 d\xi_2 d\xi_3 d\tau \\ &+ \int_0^\infty\int_0^\infty\int_0^\infty \frac{\exp\left(-\frac{||\xi-\mathbf{x}||^2}{4\alpha(\tau-t_0)}\right)}{(4\pi\alpha(\tau-t_0))^{\frac{3}{2}}}T(\boldsymbol{\xi},t_0)d\xi_1 d\xi_2 d\xi_3\,, \end{aligned} \tag{3.5}$$

where ξ_1, ξ_2 and ξ_3 are the components of the integration dummy vector $\boldsymbol{\xi}$. Based on the nature of the delta Dirac function [10, 12] the expression above can be simplified to:

$$\begin{aligned} T^{\text{analytic}}(\mathbf{x},t) = &\int_0^t \frac{\exp\left(-\frac{||\mathbf{x}-\mathbf{v_s}(\tau-t_0)-\mathbf{x_0}||^2}{4\alpha(\tau-t)}\right)}{(4\pi\alpha(\tau-t))^{\frac{3}{2}}}\frac{AP}{\rho c_p}d\tau \\ &+ \int_0^\infty\int_0^\infty\int_0^\infty \frac{\exp\left(-\frac{||\xi-\mathbf{x}||^2}{4\alpha(\tau-t_0)}\right)}{(4\pi\alpha(\tau-t_0))^{\frac{3}{2}}}T(\boldsymbol{\xi},t_0)d\xi_1 d\xi_2 d\xi_3 \end{aligned} \tag{3.6}$$

This continuous expression can be a very difficult if not impossible to solve, because of the complex integrals involved, and is thus not practical to use for general cases. Therefore, a discretization of the laser will be done by discretizing the laser path into a superposition of multiple point sources. An

illustration of this discretization can be seen in figure 3.6 for the similar circular path to be analyzed in this thesis. If the laser is discretized into J number of sources, the new governing equation becomes:

$$\frac{\partial T}{\partial t} = \alpha \nabla^2 T + \sum_{j=1}^{J} \frac{A Q_s^j}{\rho c_p} \delta(\mathbf{x} - \mathbf{x_s}^j) \delta(t - t_0^j) \,, \tag{3.7}$$

where Q_s^j is the energy per meter of each discretized source. The heat generation per meter P of the laser and the energy per meter of each discretized source Q_s^j have the following relation:

$$Q_s^j = P \Delta t \,. \tag{3.8}$$

Each disrectized source is modelled as a delta Dirac function $\delta(\mathbf{x} - \mathbf{x_s}^j)\delta(t - t_0^j)$, that is activated at location $\mathbf{x} = \mathbf{x_s}^j$ and time $t = t_0^j$. The value of the energy per meter P, the absorbtivity A, the laser scan velocity v_s and the material parameters (of the material Ti-6Al-4V, taken from [9]) k, c_p and ρ are listed in table 3.2. These parameters are also used by [2]. Now it is clear how the continuous laser is discretized into multiple point sources, it is important to know what the geometric parameters of the laser scan are.

P	A	v_s	k	c_p	ρ
400 W/m	0.818	0.3 m/s	42 W/mK	990 J/kgK	4420 kg/m^3

Table 3.2: Material and some laser parameters

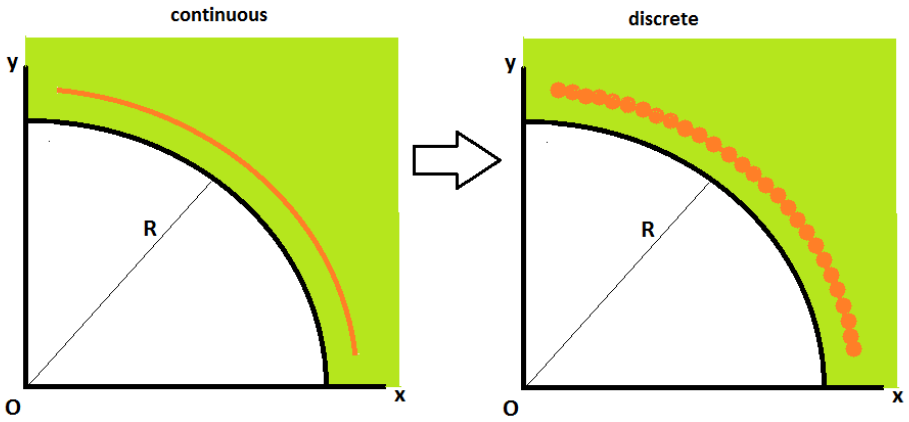

Figure 3.6: The continuous scan can be approximated by a superposition of discretized point sources.

3.3.2. The geometrical parameters of the laser scan

The discretized sources are a certain distance away from each other. Each source is activated at its own activation position $\mathbf{x_s}^j$ and at its own activation time t_0^j. At each new time increment a new source point is activated a distance $v_s \Delta t$ away from the previous one. Because the laser scn follows a circular path, it would be more convenient to relate the scanning velocity v_s to an angular velocity ω as follows:

$$\omega = \frac{v_s}{r_s} \,. \tag{3.9}$$

As explained, an thermal image will be used, which means that each source will have an image. Each source and its image will be activated at the same time. That means that the moving laser scan will have a moving 'image laser scan' that has an 'image velocity' v_i. This image should have the same

angular velocity as the laser. This gives us the following relation between the image velocity and the laser velocity:

$$\frac{v_s}{r_s} = \frac{v_i}{r_i} \,. \tag{3.10}$$

This gives the following expression for v_i:

$$v_i = v_s \frac{v_i}{r_i} \,. \tag{3.11}$$

The image velocity v_i should be interpreted as the distance between successive image source divided by the time step. For equidistant imaging the image velocity is denoted as v_e, and for inverse imaging as v_{inv}. These two velocities are defined as:

$$v_e = v_s \frac{r_e}{r_s} \tag{3.12}$$

$$v_{\text{inv}} = v_s \frac{r_{\text{inv}}}{r_s} \,. \tag{3.13}$$

Furthermore, it is more convenient to use cylindrical coordinates, because the laser has a circular path. The laser will be activated at the plane $z = 0$. The position vector of each point source j will be denoted as $\mathbf{x_s}^j$. This vector can be expressed in cylindrical coordinates as follows:

$$\begin{aligned} \mathbf{x_s}^j &= [r_s^j \cos(\theta_s^j), r_s^j \sin(\theta_s^j), 0]^T \\ &= [r_s^j \cos(\theta_0 + \omega j \Delta t), r_s^j \sin(\theta_0 + \omega j \Delta t), 0]^T \,, \end{aligned} \tag{3.14}$$

where r_s^j is the radius of source point j, θ_s^j is the angle at which each source is activated and θ_0 is the angle at which the first source is activated. Because the scanning path is circular, it is evident that r_s^j for each source is equal to the constant value of the scanning radius r_s, mentioned in table 3.1.

In figure 3.7 one can see an illustration of the path of the laser. The starting angle θ_0 is at the point where the laser is a distance H_c apart from the x-axis. The final angle θ_s^J is when the last source J is activated. This angle is reached when the laser is a distance H_c apart from the y-axis. In figure 3.7 one can see that based on symmetry, the starting and final angles have the following relation:

$$\theta_J = 90^o - \theta_0 \,. \tag{3.15}$$

Based on figure 3.7, the starting angle is calculated as follows:

$$\theta_0 = \sin^{-1}\left(\frac{H_c}{R \pm H_c}\right) . \tag{3.16}$$

In the argument of the inverse sine, one can see a ± sign. This sign is positive for a concave boundary and negative for a convex boundary. In table 3.3 one can find the values of ω, θ_0 and θ_J for both concave and convex boundaries.

As can be seen in equation 3.14 each new activated source is shifted at an angle $\omega \Delta t$ away from the previous activated source, and is shifted $\omega j \Delta t$ form the first source. This is illustrated in figure 3.8 for a concave boundary.

Knowing what the physical and geometrical parameters of the laser are, it is now possible to determine how the point sources should be distributed.

ω (concave)	ω (convex)	θ_0 (concave)	θ_J (concave)	θ_0 (convex)	θ_J (convex)
15.6^o s^{-1}	19.1^o s^{-1}	5.21^o	84.79^o	6.37^o	83.63^o

Table 3.3: The angular velocity and starting and ending angles

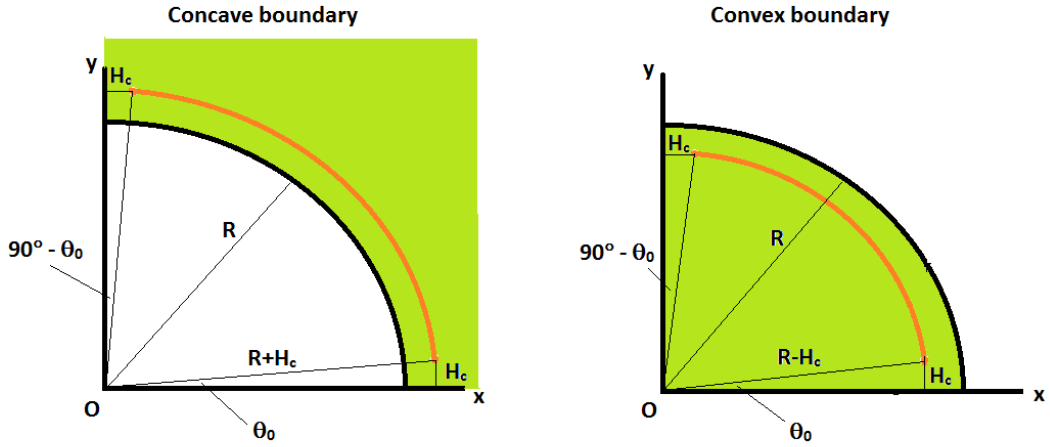

Figure 3.7: The scan has a circular path that starts at θ_0, when the laser scan has a distance H_c to both the cylindrical boundary boundary and the x-axis. The laser scan ends when the laser scan has a distance H_c to both the boundary and the y-axis. Both concave and convex boundaries are illustrated.

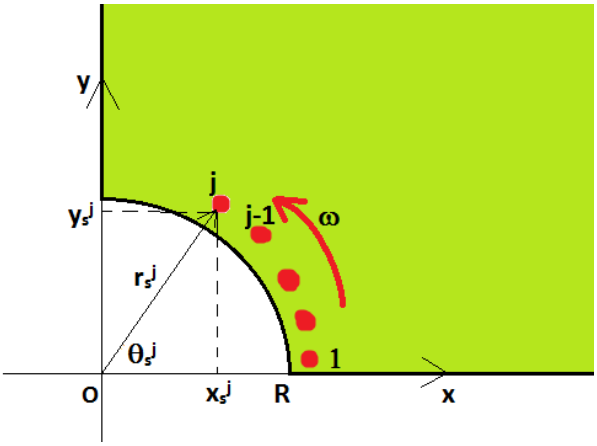

Figure 3.8: The scan has a circular path and is discretized into multiple sources. Each source j is activated at time t_0^j at radius r_s^j and angle θ_s^j. For a circular path the radius is constant: $r_s^j = r_s$.

3.3.3. Activation times and distribution of the point sources

The temperature profile that is caused by the laser will be modelled as a super position of point sources. At $t = I\Delta t$ the temperature profile is the superposition of the temperature profiles of each source T^j form the first source up until the J^{th} source (for $I > J$):

$$T(\boldsymbol{x}, I\Delta t) = \sum_{j=1}^{J} T^j(\boldsymbol{x}, I\Delta t) \tag{3.17}$$

Where $T^j(\mathbf{x}, t)$ is defined as:

$$T^j(\mathbf{x}, t) = \frac{AQ_s^j}{\rho c_p} \frac{\exp\left(-\frac{||\mathbf{x}-\mathbf{x_s}^j||^2}{4\alpha(t-t_0^j)}\right)}{(4\alpha\pi(t-t_0^j))^{\frac{3}{2}}} H(t-t_0^j) \tag{3.18}$$

The function $H(t-t_0^j)$ is a Heaviside step-function that has a value of 1 for $t \geq t_0$ and zero at other time instances. Furthermore, it is clear that at time $t = t_0^j$, T^j has a singularity for source j at $\mathbf{x} = \boldsymbol{x_s}$. In order

to avoid this singularity a time shift will be introduced, that activates the point source at time τ_0^j [2, 3]. This new activation time is such that it allows the laser to have a spot radius $r_L = 35\mu$m [3]. The new activation time [2, 3] is therefore:

$$\tau_0^j = t_0^j - \frac{r_L^2}{4\alpha} \tag{3.19}$$

Having dealt with the singularities by using a time shift, it is also important to look at another aspect of approximating the laser scan: the distribution of the point sources. In order to have an appropriate approximation of the laser, the source points should be distributed well. Discretization gives namely a certain error, and therefore not every number of sources gives a good approximation. In order to get a proper approximation of the laser scan, the source density ρ_s, the number of sources per unit length, has to have an appropriate number [2]. The source density is defined as [2]:

$$\rho_s = \frac{1}{v_s \Delta t} \, . \tag{3.20}$$

Based on the studies of [2] a source density of 67 sources per millimeter approximates a straight line with a difference of 3.5% from the exact solution. This source density gives a time step of $\Delta t = 5 \times 10^{-5}$ s. These will be chosen as source density and time step in our thesis.

Up until now, it is explained what the geometrical parameters are of the domain and laser, the physical quantities of the material and laser and the discretization method of the laser into multiple sources. It is also shown how an inverse image for a single source is constructed. The next step is to derive the boundary flux for the inverse imaging method by means of super position of the temperature fields of the discretized sources.

3.4. The boundary flux for inverse imaging

The final step in this chapter is to derive the expression of the boundary flux for inverse imaging in the thermal modelling of the LBPF-process. This boundary flux will be the input for the numerical correction field and has to be smooth enough to be captured by a coarser mesh than is used in modulated equidistant imaging. The first thing that will be explained is how the boundary flux is derived in general from the temperature. Next, the expression of the temperature field will be shown, based on the information that is mentioned before in this chapter. After that the boundary fluxes will be derived. At the end, the method of analysis in the next chapter will be shortly explained.

3.4.1. Boundary flux for circular boundaries

The boundary flux is given by the inner product of the normal vector $\mathbf{n}$ and the flux vector $\mathbf{q}$, that are both illustrated in figure 2.2. As explained in chapter 2, the heat flux vector, is proportional to the gradient of the temperature. The boundary flux can therefore be expressed as the product of the absolute value of the gradient of the temperature and the direction cosine of the gradient [8, 9]:

$$q(\mathbf{x}, t) = -k \nabla T(\mathbf{x}, t) \cdot \mathbf{n}(\mathbf{x}) \tag{3.21}$$

$$= -k ||\nabla T(\mathbf{x}, t)|| \cos(\theta_n) \, , \tag{3.22}$$

where θ_n is the angle between the normal vector and the gradient. As can be seen in figure 3.9, the direction of the normal vector is parallel to the direction of the variable r. Therefore the flux at the circular boundary can be easily calculated by taking the derivative of the temperature with respect to r. The fact that the normal vector and the direction of the variable r are parallel also means that the directional cosine $\cos(\theta_n)$ is either equal to 1 or -1, depending on if the boundary is concave or convex. For a concave boundary the boundary flux is therefore:

$$q(R, \theta, z, t) = k \frac{\partial T}{\partial r}\Big|_{r=R} \, . \tag{3.23}$$

For a convex boundary the boundary flux is:

$$q(R, \theta, z, t) = -k \frac{\partial T}{\partial r}\Big|_{r=R} \, . \tag{3.24}$$

In order to calculate the derivative of the temperature, the expression of the temperature should be known.

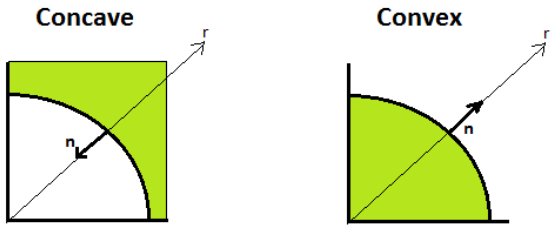

Figure 3.9: The normal vector is in the positive direction of r for concave boundaries. For convex boundaries it is however in the negative direction.

3.4.2. The temperature profile

Before one looks at the expression of the temperature profile of inverse imaging, it is worth to know how the temperature profile looks like when no images are used and when modulated equidistant images are used. This way it is possible to have a reference when analyzing the inverse imaging method.

The temperature field when no images are used will be denoted as T_∞. When modulated equidistant images are used the temperature field will be denoted as T_e^{mod}. For inverse imaging the temperature field will be denoted as T_{inv}.

If the laser is discretized into multiple sources, the expression of T_∞ is:

$$T_\infty(r,\theta,z,t) = T_0 + \frac{AP\Delta t}{c_p\rho}\sum_{j=1}^{J}\frac{\exp\left(-\frac{r^2+r_e^2-2rr_e\cos(\theta-\theta_s^j)+z^2}{4\alpha(t-\tau_0^j)}\right)}{(4\pi\alpha(t-\tau_0^j))^{\frac{3}{2}}}H(t-\tau_0^j)\,, \tag{3.25}$$

where T_0 is the initial temperature equal to 230 K.

The expression of T_e^{mod} is:

$$T_e^{\text{mod}}(r,\theta,z,t) = T_0 + \frac{AP\Delta t}{c_p\rho}\sum_{j=1}^{J}\frac{\exp\left(-\frac{z^2}{4\alpha(t-\tau_0^j)}\right)}{(4\pi\alpha(t-\tau_0^j))^{\frac{3}{2}}}H(t-\tau_0^j)\Big(\exp\left(-\frac{r^2+r_s^2-2rr_s\cos(\theta-\theta_s^j)}{4\alpha(t-\tau_0^j)}\right)+$$
$$f_d\exp\left(-\frac{r^2+r_e^2-2rr_e\cos(\theta-\theta_s^j)}{4\alpha(t-\tau_0^j)}\right)\Big)\,. \tag{3.26}$$

Here f_d is the modulation for equidistant imaging, and is defined as:

$$f_d = \frac{v_e}{v_s}\,. \tag{3.27}$$

For a circular path, where the angular velocity is constant, as is the case in this thesis, the modulation factor can be rewritten as:

$$f_d = \frac{r_e}{r_s} \tag{3.28}$$

It should be noted that the expression of T_e^{mod} is a superposition of the temperature field of the original source and of the equidistant image source, and not only of the image source.

The temperature profile for inverse imaging T_{inv} can be expressed as:

$$T_{\text{inv}}(r,\theta,z,t) = T_0 + \frac{AP\Delta t}{c_p\rho}\sum_{j=1}^{J}\frac{\exp\Big(-\frac{z^2}{4\alpha(t-\tau_0^j)}\Big)}{(4\pi\alpha(t-\tau_0^j))^{\frac{3}{2}}}H(t-\tau_0^j)\Big(\exp\Big(-\frac{r^2+r_s^2-2rr_s\cos(\theta-\theta_s^j)}{4\alpha(t-\tau_0^j)}\Big)+ \exp\Big(-\gamma\frac{r^2+r_{\text{inv}}^2-2rr_{\text{inv}}\cos(\theta-\theta_s^j)}{4\alpha(t-\tau_0^j)}\Big)\Big). \tag{3.29}$$

It should also be noted here that the expression of T_{inv} is a superposition of the temperature field of the original source and of the inverse image, and not only of the image. In the appendix one can find the contour plots of the temperature profiles T_e^{inv} and T_{inv}, to have an idea about how the temperature profile during the scanning process looks like. The contour plots of T_e^{mod} can be seen in figure 6.1 for a concave boundary and in figure 6.3 for a convex boundary. For T_{inv} the contour plots can be seen in figure 6.2 for a concave boundary and in figure 6.4 for a convex boundary. Now the expressions of the temperature fields are known, the fluxes can be derived from them.

3.4.3. The boundary fluxes

The boundary fluxes for circular boundaries are proportional to the derivatives of the temperature with respect to the radial variable r, as is explained. When no images are used, the boundary flux q_∞ has the following expression:

$$q_\infty(R,\theta,z,t) = \mp\frac{2kAP\pi\Delta t}{c_p\rho}\sum_{j=1}^{J}H(t-\tau_0^j)(R-r_s\cos(\theta-\theta_s^j))\frac{\exp\Big(-\frac{R^2+r_s^2-2Rr_s\cos(\theta-\theta_s^j)+z^2}{4\alpha(t-\tau_0^j)}\Big)}{(4\pi\alpha(t-\tau_0^j))^{\frac{5}{2}}}. \tag{3.30}$$

The sign before the expression depends on the type of cylindrical boundary. For a concave boundary, the expression of q_∞ has a minus sign before it. If the boundary is convex, the expression of q_∞ has a plus sign. For equidistant imaging the flux q_e^{mod} is:

$$q_e^{\text{mod}}(R,\theta,z,t) = \mp\frac{2kAP\pi\Delta t}{c_p\rho}\sum_{j=1}^{J}\frac{\exp\Big(-\frac{z^2}{4\alpha(t-\tau_0^j)}\Big)}{(4\pi\alpha(t-\tau_0^j))^{\frac{5}{2}}}H(t-\tau_0^j)\times \Big((R-r_s\cos(\theta-\theta_s^j))\exp\Big(-\frac{R^2+r_s^2-2Rr_s\cos(\theta-\theta_s^j)}{4\alpha(t-\tau_0^j)}\Big)+ f_d^e(R-r_e\cos(\theta-\theta_s^j))\exp\Big(-\frac{R^2+r_e^2-2Rr_e\cos(\theta-\theta_s^j)}{4\alpha(t-\tau_0^j)}\Big)\Big). \tag{3.31}$$

The sign before the expression depends on the type of boundary, as is explained for q_∞. For inverse imaging the flux q_{inv} is:

$$q_{\text{inv}}(R,\theta,z,t) = \mp\frac{2kAP\pi\Delta t}{c_p\rho}\sum_{j=1}^{J}\frac{\exp\Big(-\frac{z^2}{4\alpha(t-\tau_0^j)}\Big)}{(4\pi\alpha(t-\tau_0^j))^{\frac{5}{2}}}H(t-\tau_0^j)\times \Big((R-r_s\cos(\theta-\theta_s^j))\exp\Big(-\frac{R^2+r_s^2-2Rr_s\cos(\theta-\theta_s^j)}{4\alpha(t-\tau_0^j)}\Big)+ \gamma(R-r_{\text{inv}}\cos(\theta-\theta_s^j))\exp\Big(-\gamma\frac{R^2+r_{\text{inv}}^2-Rr_{\text{inv}}\cos(\theta-\theta_s^j)}{4\alpha(t-\tau_0^j)}\Big)\Big). \tag{3.32}$$

The scaling factor γ brings the advantage that this expression can be simplified to:

$$q_{\text{inv}}(R,\theta,z,t) = \mp \frac{2kAP\pi\Delta t}{c_p\rho} \sum_{j=1}^{J} \frac{\exp\left(-\frac{z^2}{4\alpha(t-\tau_0^j)}\right)}{(4\pi\alpha(t-\tau_0^j))^{\frac{5}{2}}} H(t-\tau_0^j)\times$$
$$\left(((1+\gamma)R - 2r_s\cos(\theta-\theta_s^j))\exp\left(-\frac{R^2+r_s^2-2Rr_s\cos(\theta-\theta_s^j)}{4\alpha(t-\tau_0^j)}\right)\right). \tag{3.33}$$

The sign before the expression depends on the type of boundary, as explained for q_∞ and q_e^{mod}. Now the expressions of the boundary fluxes are available, it is possible to analyze them.

3.4.4. Methodology of the analysis of the boundary flux

In the next chapter the smoothness flux of the inverse imaging will be analyzed and compared to the smoothness of the flux of the modulated equidistant imaging. This will be done by showing the curves along the boundary at the height $z = 0$, and analyzing them visually for their smoothness.

4

Results and discussion

In this chapter the smoothness of the flux for inverse imaging (i.e. q_{inv} in equation 3.33) will be compared to that of modulated equidistant imaging (i.e. q_e^{mod} in equation 3.31). All the simulations will be done for both concave and convex boundaries. The fluxes will be plotted as function of the angle along the boundary. After the simulations are shown and analyzed, their results will be discussed and explained.

4.1. Results

This section contains the simulations of the boundary fluxes for both concave and convex imaging. In order to give a reference q_∞ will also be shown. Their smoothness will be analyzed visually.

4.1.1. Concave boundary

For a concave boundary the boundary fluxes as function of the angle θ can be seen in figure 4.1 for no imaging q_∞, modulated equidistant imaging q_e^{mod} and inverse imaging q_{inv}, for different time steps. It is clear that both imaging method reduce the large peak of q_∞. In figure 4.2 we take a closer look at only the fluxes that use an imaging method. There, two clear significant large peaks can be seen for modulated equidistant imaging, while q_{inv} seems to have only one significant large peak, similar to q_∞, but smaller and with a different sign. The flux for inverse imaging appears to be smoother than the flux for modulated equidistant imaging. The latter one has namely a large jump.

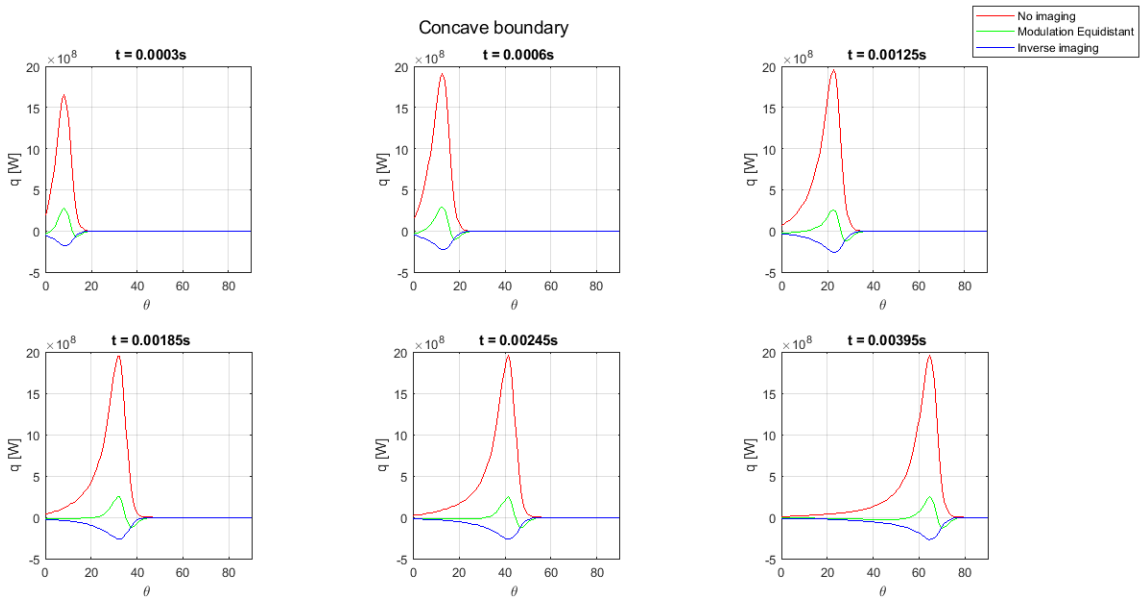

Figure 4.1: The boundary fluxes q_∞ (red), q_e^{mod} (green) and q_{inv} (blue) for a concave boundary as a function of the angle of the circular boundary, for multiple time instances during the scanning. In the next figure the fluxes q_e^{mod} and q_{inv} are zoomed in on.

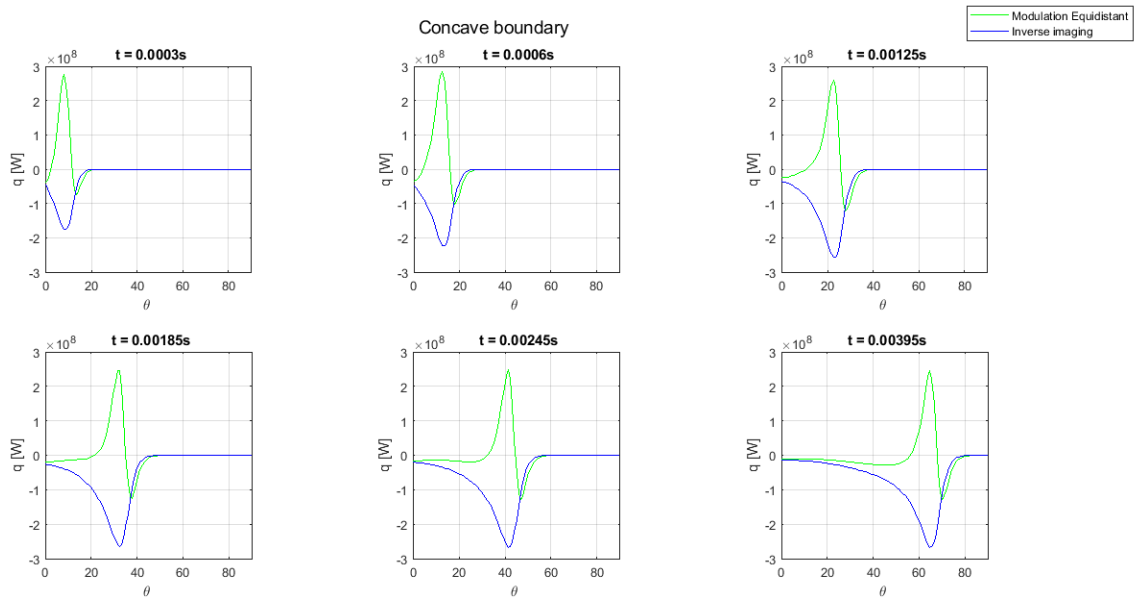

Figure 4.2: Zooming in on q_e^{mod} and q_{inv} from figure 4.1. The boundary fluxes q_e^{mod} (green) and q_{inv} (blue) for a concave boundary as a function of the angle of the circular boundary, for multiple time instances during the scanning.

4.1.2. Convex boundary

For a convex boundary the boundary fluxes as function of the angle θ can be seen in figure 4.3 for no imaging q_∞, modulated equidistant imaging q_e^{mod} and inverse imaging q_{inv}, for different time steps. As was the case for a concave boundary, it is also clear for a convex boundary that both imaging method reduce the large peak of q_∞. In figure 4.4 a closer look is taken on only the fluxes that use an imaging method. Like the concave boundary, two clear significant large peaks for the convex boundary can be seen for equidistant imaging, while q_{inv} seems to have only one significant large peak, similar to q_∞, but smaller. It is apparent that the flux for inverse imaging in convex boundaries is also smoother than the

flux for modulated equidistant imaging. A similar jump as in the concave case can be seen in the latter one.

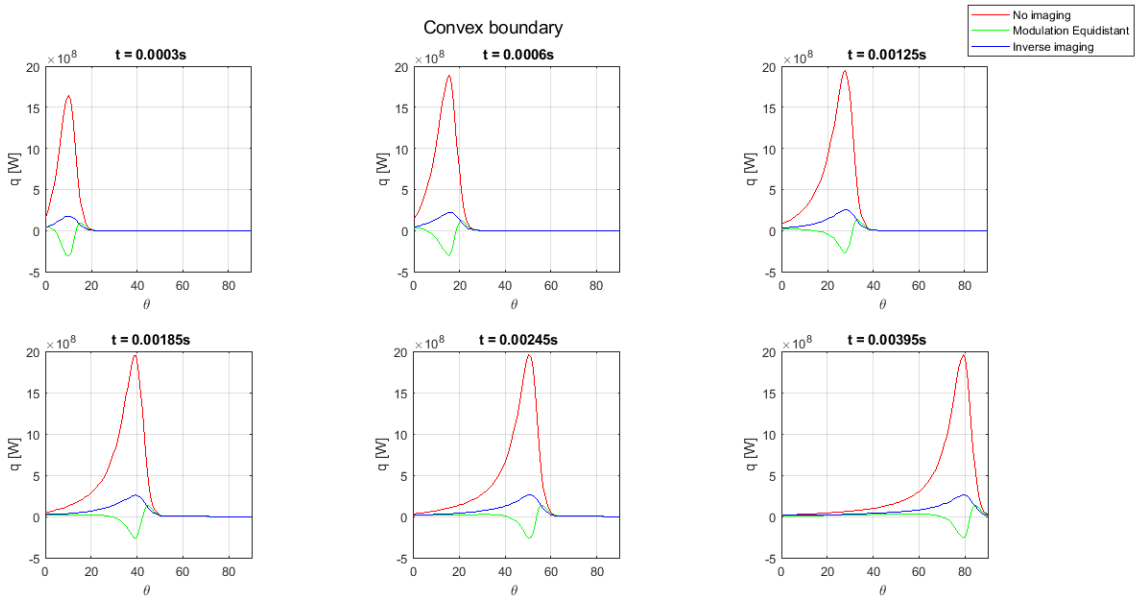

Figure 4.3: The boundary fluxes q_∞ (red), q_e^{mod} (green) and q_{inv} (blue) for a convex boundary as a function of the angle of the circular boundary, for multiple time instances during the scanning. In the next figure the fluxes q_e^{mod} and q_{inv} are zoomed in on.

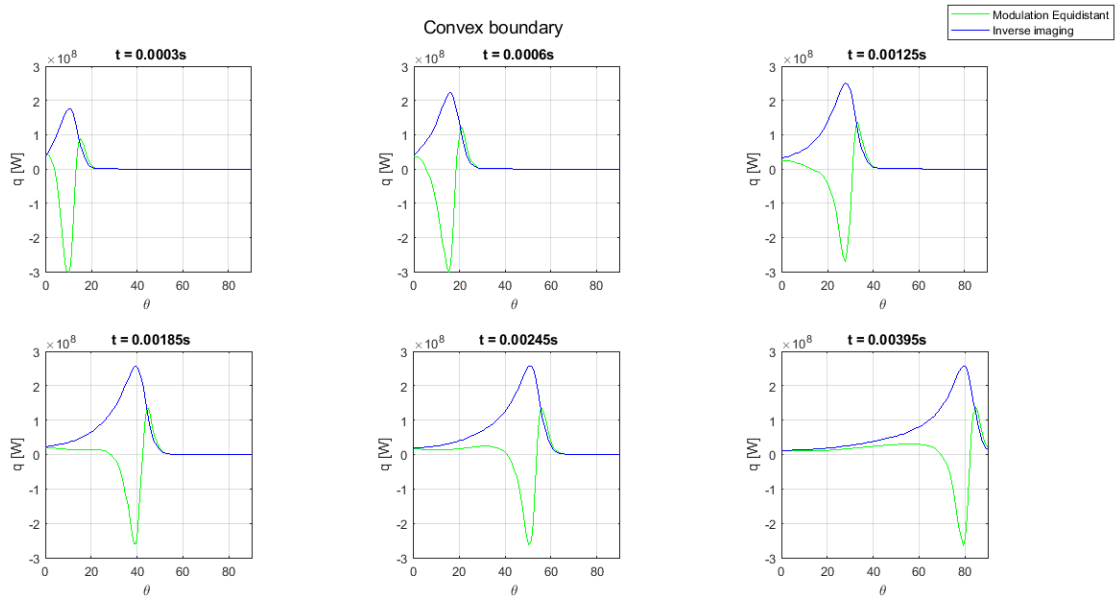

Figure 4.4: Zooming in on q_e^{mod} and q_{inv} from figure 4.3. The boundary fluxes q_e^{mod} (green) and q_{inv} (blue) for a convex boundary as a function of the angle of the circular boundary, for multiple time instances during the scanning.

4.2. Discussion

The simulations show that for both concave and convex boundaries the inverse imaging gives a smoother boundary flux than the modulated equidistant imaging. This means that at least where q_∞ has a significant large value, the imaging term in inverse image reflects q_∞ better than equidistant imaging. What is meant by reflection is measure at which the flux of the image term 'compensates' the flux of the

source at the boundary. To understand this better, the imaging terms for both imaging methods will be investigated, and a measure for the flux reflection will be explored.

4.2.1. Investigating the imaging terms

The imaging terms reflect the flux of the original source term. Both imaging methods contain q_∞ as a term:

$$q_e^{\text{mod}} = q_\infty + \tilde{q}_e^{\text{mod}} \tag{4.1}$$

$$q_{\text{inv}} = q_\infty + \tilde{q}_{\text{inv}} \,, \tag{4.2}$$

where $\tilde{q}_e^{\text{mod}}$ is the image term for modulated equidistant imaging and $\tilde{q}_{\text{inv}}$ is the image term for inverse imaging. Combining the above equations with equations 2.26, 2.27, 3.30 3.31 and 3.32 the imaging terms can be expressed as:

$$\tilde{q}_e^{\text{mod}} = \mp \frac{2kAP\pi\Delta t}{c_p\rho} \sum_{j=1}^{J} \frac{\exp\left(-\frac{z^2}{4\alpha(t-\tau_0^j)}\right)}{(4\pi\alpha(t-\tau_0^j))^{\frac{5}{2}}} H(t-\tau_0^j) f_d(R - r_e\cos(\theta-\theta_s^j)) \exp\left(-\frac{R^2 + r_e^2 - Rr_e\cos(\theta-\theta_s^j)}{4\alpha(t-\tau_0^j)}\right)\Big) \tag{4.3}$$

$$\tilde{q}_{\text{inv}} = \mp \frac{2kAP\pi\Delta t}{c_p\rho} \sum_{j=1}^{J} \frac{\exp\left(-\frac{z^2}{4\alpha(t-\tau_0^j)}\right)}{(4\pi\alpha(t-\tau_0^j))^{\frac{5}{2}}} H(t-\tau_0^j)(\gamma R - r_s\cos(\theta-\theta_s^j)) \exp\left(-\frac{R^2 + r_s^2 - Rr_s\cos(\theta-\theta_s^j)}{4\alpha(t-\tau_0^j)}\right)\Big) \,. \tag{4.4}$$

As a reminder we repeat that the minus sign in these expressions is for concave boundaries and a plus sign is for convex boundaries.

For concave boundaries one can see in figure 4.5 the plots of q_∞, $\tilde{q}_e^{\text{mod}}$ and q_e^{mod}, and in figure 4.6 the plots of q_∞, $\tilde{q}_{\text{inv}}$ and q_{inv}. For convex boundaries one can see in figure 4.7 the plots of q_∞, $\tilde{q}_e^{\text{mod}}$ and q_e^{mod}, and in figure 4.8 the plots of q_∞, $\tilde{q}_{\text{inv}}$ and q_{inv}. The figures of the image terms do not clearly show how inverse imaging reflects the flux from q_∞ different from modulated equidistant imaging. Both seem to have a reflecting effect to begin with, which can be seen by the fact that the imaging terms have a large peak with the opposite sign around the large peak of the source flux q_∞. Also the height of the peaks of the image terms seam to have a reasonable size to reduce the peak of the source. The total field q_e^{mod} and q_{inv} clearly show that the source flux is reduced by the image flux.

However it cannot be seen from the figures why q_e^{mod} seems to have large fluctuations, which makes it less smooth, and why q_{inv} does not have these fluctuations. In order to understand this better, we will dive deeper in analyzing the reflection, by studying the reflection behaviour for a single source.

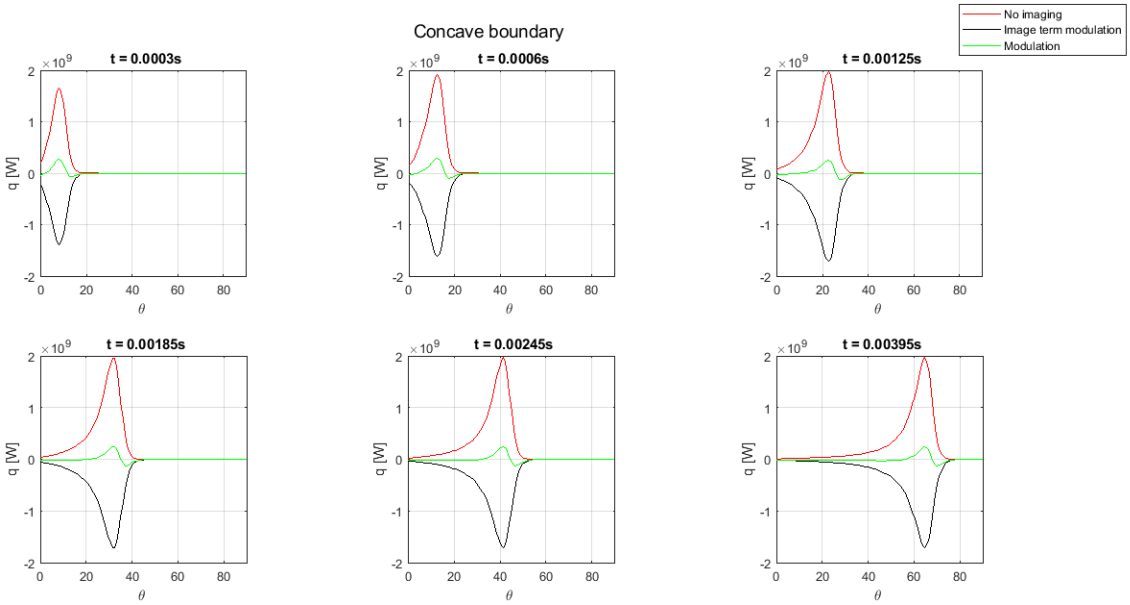

Figure 4.5: Boundary fluxes for concave boundaries. The red curve represents q_∞. The image term for modulated equidistant imaging $\tilde{q}_e^{\text{mod}}$ is represented by the black curve. The total field q_e^{mod} is the green curve.

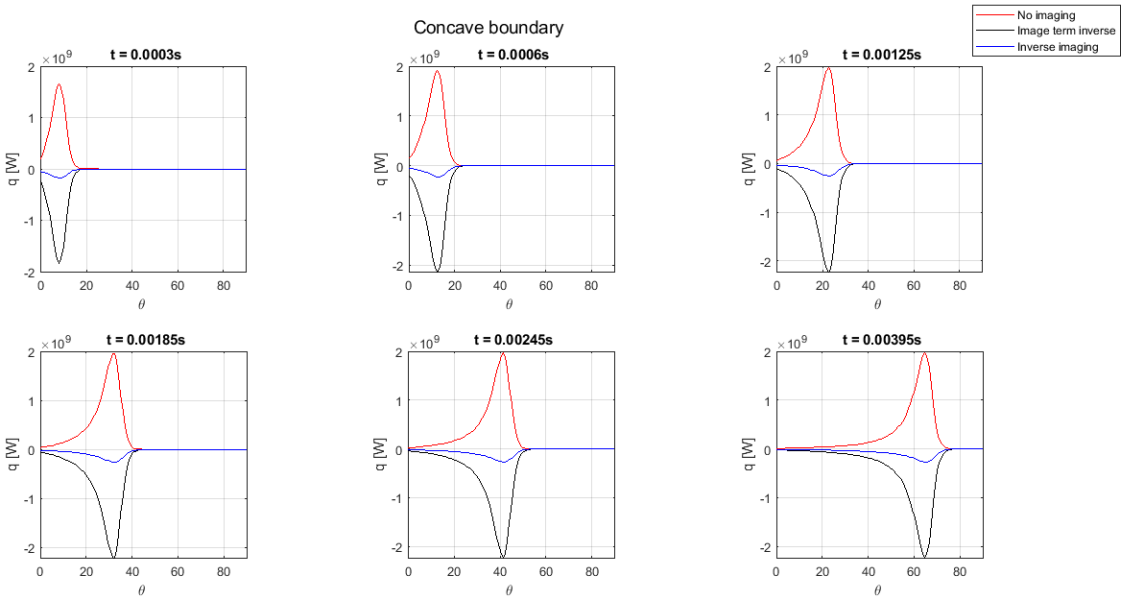

Figure 4.6: Boundary fluxes for concave boundaries. The red curve represents q_∞. The image term for modulated equidistant imaging $\tilde{q}_{\text{inv}}$ is represented by the black curve. The total field q_{inv} is the green curve.

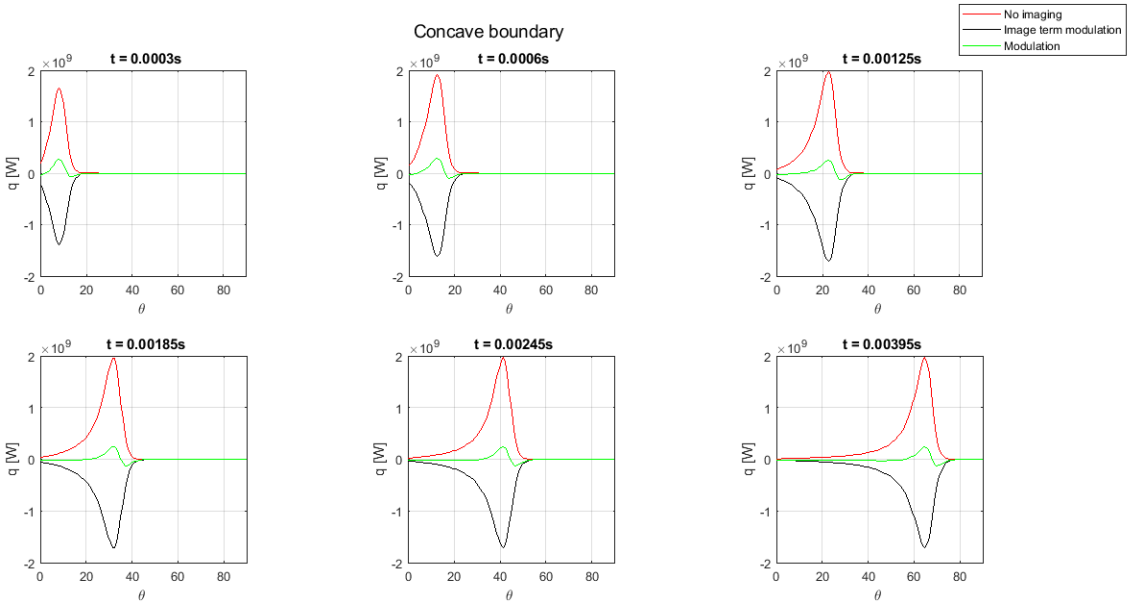

Figure 4.7: Boundary fluxes for convex boundaries. The red curve represents q_∞. The image term for modulated equidistant imaging $\tilde{q}_e^{\text{mod}}$ is represented by the black curve. The total field q_e^{mod} is the green curve.

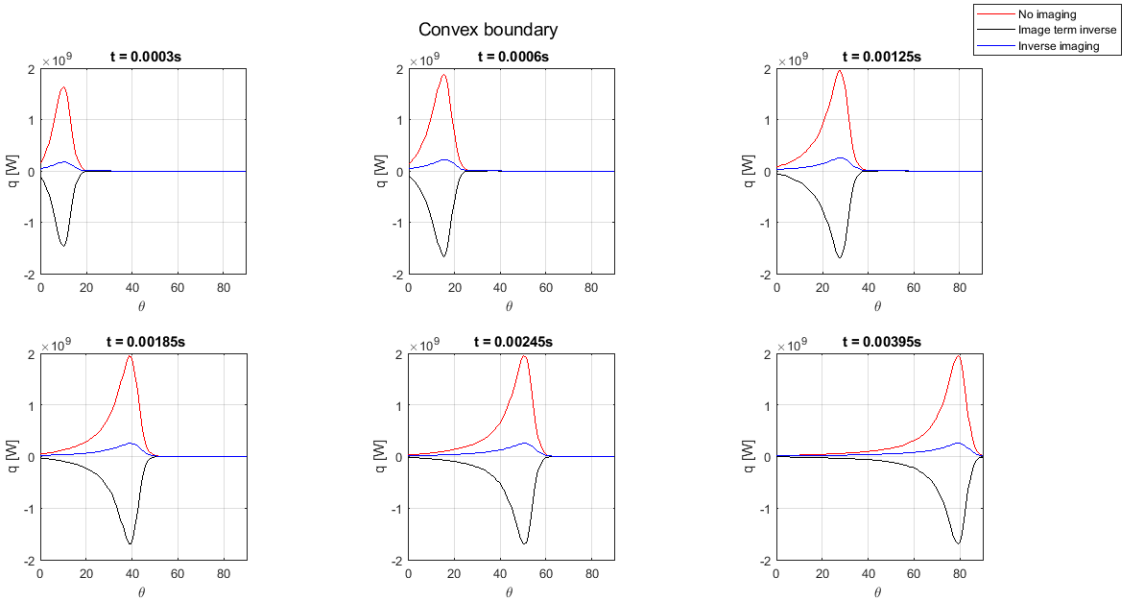

Figure 4.8: Boundary fluxes for convex boundaries. The red curve represents q_∞. The image term for modulated equidistant imaging $\tilde{q}_{\text{inv}}$ is represented by the black curve. The total field q_{inv} is the green curve.

4.2.2. Reflection ratio

As is explained, the laser is discretized into multiple sources. If an imaging method is used, each of these sources is reflected by its image. Therefore, in order to understand more about how the fluxes are reflected in the simulation of the laser scan, single sources will be analyzed.

The flux for a single source with no images for a source j is defined as:

$$\hat{q}_\infty = \mp \frac{2kAP\pi\Delta t}{c_p\rho} \frac{\exp\left(-\frac{z^2}{4\alpha(t-\tau_0^j)}\right)}{(4\pi\alpha(t-\tau_0^j))^{\frac{5}{2}}} H(t-\tau_0^j)(R - r_s\cos(\theta-\theta_s^j)) \exp\left(-\frac{R^2 + r_s^2 - Rr_s\cos(\theta-\theta_s^j)}{4\alpha(t-\tau_0^j)}\right)\Big). \tag{4.5}$$

When modulated equidistant imaging is applied, the image flux of a single source is:

$$\hat{q}_{\text{mod,e}} = \mp \frac{2kAP\pi\Delta t}{c_p\rho} \frac{\exp\left(-\frac{z^2}{4\alpha(t-\tau_0^j)}\right)}{(4\pi\alpha(t-\tau_0^j))^{\frac{5}{2}}} H(t-\tau_0^j) f_d(R - r_e\cos(\theta-\theta_s^j)) \exp\left(-\frac{R^2 + r_e^2 - Rr_e\cos(\theta-\theta_s^j)}{4\alpha(t-\tau_0^j)}\right)\Big). \tag{4.6}$$

When inverse imaging is applied, the image flux of a single source is:

$$\hat{q}_{\text{inv}} = \mp \frac{2kAP\pi\Delta t}{c_p\rho} \frac{\exp\left(-\frac{z^2}{4\alpha(t-\tau_0^j)}\right)}{(4\pi\alpha(t-\tau_0^j))^{\frac{5}{2}}} H(t-\tau_0^j)(-r_s\cos(\theta-\theta_s^j)) \exp\left(-\frac{R^2 + r_s^2 - Rr_s\cos(\theta-\theta_s^j)}{4\alpha(t-\tau_0^j)}\right)\Big). \tag{4.7}$$

We will define a ratio for the reflection of the boundary flux, the reflection ratio Φ. For convex boundaries this ratio for modulated equidistant imaging $\Phi_{\text{mod,e}}$ is defined as:

$$\begin{aligned}\Phi_{\text{mod,e}} &= \frac{\hat{q}_{\text{mod,e}}}{\hat{q}_\infty} \\ &= f_d \frac{R - r_e\cos(\theta-\theta_s^j)}{R - r_s\cos(\theta-\theta_s^j)} \exp\left(-\frac{r_e^2 - r_s^2 - R(r_e - r_s)\cos(\theta-\theta_s^j)}{4\alpha(t-\tau_0^j)}\right).\end{aligned} \tag{4.8}$$

The reflection ratio for inverse imaging Φ_{inv} is defined as:

$$\begin{aligned}\Phi_{\text{inv}} &= \frac{\hat{q}_{\text{mod,e}}}{\hat{q}_\infty} \\ &= \frac{\gamma R - r_s\cos(\theta-\theta_s^j)}{R - r_s\cos(\theta-\theta_s^j)}\end{aligned} \tag{4.9}$$

Because for convex boundaries the boundary radius is larger than the radius to the source (i.e. $R \geq r_s$), the denominator of the ratios does not become zero. However, for concave boundaries the boundary radius is always smaller than the radius to the point source (i.e. $R \leq r_s$). That means that the denominator of Φ becomes zero at certain angles, which lead to singularities. Therefore, the inverse of the reflection ratio Φ^{-1} is more appropriate for concave boundaries:

$$\begin{aligned}\Phi_{\text{mod,e}}^{-1} &= \frac{\hat{q}_\infty}{\hat{q}_{\text{mod,e}}} \\ &= \frac{1}{f_d} \frac{R - r_s\cos(\theta-\theta_s^j)}{R - r_e\cos(\theta-\theta_s^j)} \exp\left(-\frac{r_s^2 - r_e^2 - R(r_s - r_e)\cos(\theta-\theta_s^j)}{4\alpha(t-\tau_0^j)}\right),\end{aligned} \tag{4.10}$$

and:

$$\begin{aligned}\Phi_{\text{inv}}^{-1} &= \frac{\hat{q}_{\text{mod,e}}}{\hat{q}_\infty} \\ &= \frac{R - r_s\cos(\theta-\theta_s^j)}{\gamma R - r_s\cos(\theta-\theta_s^j)}.\end{aligned} \tag{4.11}$$

In all the expressions of Φ and Φ^{-1} a phase difference $\theta - \theta_s^j$ can be found. This phase difference will be defined as:

$$\Delta\theta = \theta - \theta_s^j \,. \tag{4.12}$$

Since the problem in this thesis is only defined on a quarter circle, the minimum value of $\Delta\theta$ is -90^o, and the maximum value is 90^o. When $\Delta\theta$ is zero, we are at the angle where the source and image are placed $\theta = \theta_s^j$. The reflection ratios and their inverses can therefore be expressed as:

$$\Phi_{\text{mod,e}} = f_d \frac{R - r_e \cos\Delta\theta}{R - r_s \cos\Delta\theta} \exp\Big(- \frac{r_e^2 - r_s^2 - R(r_e - r_s)\cos\Delta\theta}{4\alpha(t - \tau_0^j)} \Big) \tag{4.13}$$

$$\Phi_{\text{mod,e}}^{-1} = \frac{1}{f_d} \frac{R - r_s \cos\Delta\theta}{R - r_e \cos\Delta\theta} \exp\Big(- \frac{r_s^2 - r_e^2 - R(r_s - r_e)\cos\Delta\theta}{4\alpha(t - \tau_0^j)} \Big) \tag{4.14}$$

$$\Phi_{\text{inv}} = \frac{\gamma R - r_s \cos\Delta\theta}{R - r_s \cos\Delta\theta} \tag{4.15}$$

$$\Phi_{\text{inv}}^{-1} = \frac{R - r_s \cos\Delta\theta}{\gamma R - r_s \cos\Delta\theta} \,. \tag{4.16}$$

All these ratios (or their inverse) have in common that if they have a value of -1, the source flux is perfectly reflected by the image.

If the value of $\Phi_{\text{mod,e}}$ and Φ_{inv} is between 0 and -1, the flux is partially reflected. A value larger than 0 means that the flux is not reflected, and that the image even adds flux at the boundary, which can make the boundary flux even more steeper. A value that is lower than -1 means that the image reflects more than is required.

For the values of $\Phi_{\text{mod,e}}^{-1}$ and Φ_{inv}^{-1} there are different criteria. A value between 0 and -1 means that the image reflects more heat than required. A value smaller than -1 means that the image reflects the heat of the source partially. A value larger than 0 means that the heat is not reflected at all, and that the image even adds flux at the boundary.

In figure 4.9 one can see how Φ^{-1} changes as a function of $\Delta\theta$. Because the peak of q_∞ is at $\Delta\theta = 0$, the most interesting part to analyze for reflection is at this point and close to it, since the most significant amounts of heat are released near this point. Angles that are farther away from $\Delta\theta = 0$ are not so important, since the value of q_∞ decays rapidly farther away from the heat source as can be seen in figures 4.7 and 4.8. Therefore, we will only analyze the region close to $\Delta\theta = 0$.

The inverse ratio $\Phi_{\text{mod,e}}^{-1}$ in figure 4.9 seems to intersect the line $\Phi_{\text{mod,e}}^{-1} = -1$ twice, when it is close to $\Delta\theta = 0$. Keep in mind that a value of -1 means total reflection, a value between 0 and -1 means that too much is reflected, and a value smaller than -1 means that the flux is partially reflected. This means that for modulated equidistant imaging in concave boundaries, the image term fluctuates between reflecting too much and reflecting partially near $\Delta\theta = 0$. A fluctuation can also be seen for convex boundaries in modulated equidistant imaging, as can be seen in figure 4.10 for $\Phi_{\text{mod,e}}$. This explains why the boundary flux of the total field for modulated equidistant imaging jumps from a positive to a negative value, as can be seen in figures 4.1, 4.2, 4.3 and 4.4.

For inverse imaging we see that both Φ_{inv}^{-1} for concave boundaries and Φ_{inv} for convex boundaries stay between 0 and -1 around the value $\Delta\theta = 0$. Which means for concave boundaries that the flux is always partially reflected around the peak, and for convex boundaries the flux is always reflecting too much. In all cases fluctuations around the peak are absent, and because the reflection ratio or its inverse are negative around the peak, a reduction of the peak flux is always done. This explains why inverse imaging has a smoother boundary flux than modulated equidistant imaging.

The location of the inverse point and factor γ make it possible for the reflection ratio and its inverse to keep their values above the value of -1 and never intersect it. This will become more clear if we

calculate the value of Φ_{inv}^{-1} and Φ_{inv} are calculated at the $\Delta\theta = 0$. Using equations 2.26, 2.27 4.15 and 4.16 and the definition of $r_s = R \pm H_c$, one gets for Φ_{inv}^{-1} (concave boundaries):

$$\begin{aligned}
\Phi_{\text{inv}}^{-1}(\Delta\theta = 0) &= \frac{R - r_s}{\gamma R - r_s} \\
&= \frac{-H_c}{\frac{r_s^2}{R} - r_s} \\
&= \frac{-H_c}{r_s(\frac{r_s}{R} - 1)} \\
&= R\frac{-H_c}{r_s(r_s - R))} \\
&= R\frac{-H_c}{r_s H_c} \\
&= -\frac{R}{R + H_c} \geq -1 \,.
\end{aligned}$$

For convex boundaries Φ_{inv}^{-1} at the peak point gives:

$$\begin{aligned}
\Phi_{\text{inv}}(\Delta\theta = 0) &= \frac{\gamma R - r_s}{R - r_s} \\
&= \frac{r_s^2}{R} - r_s\frac{H_c}{} \\
&= \frac{r_s(\frac{r_s}{R} - 1)}{H_c} \\
&= \frac{r_s(r_s - R))}{RH_c} \\
&= \frac{-r_s H_c}{RH_c} \\
&= -\frac{R - H_c}{R} \geq -1 \,.
\end{aligned}$$

The reflection ratio and its inverse for modulated equidistant imaging has always a value lower than -1 at the peak point $\Delta\theta = 0$. Using equations 4.15 and 4.16 and the definitions of $r_s = R \pm H_c$, $r_e = 2R - r_s$ and $f_d = \frac{r_e}{r_s}$, the value of $\Phi_{\text{mod,e}}^{-1}$ for concave boundaries at the peak point is:

$$\begin{aligned}
\Phi_{\text{mod,e}}^{-1}(\Delta\theta = 0) &= \frac{1}{f_d}\frac{R - r_s}{R - r_e} \\
&= \frac{r_s}{r_e}\frac{-H_c}{H_c} \\
&= -\frac{r_s}{r_e} \leq -1 \,.
\end{aligned}$$

For convex boundaries, the value of $\Phi_{\text{mod,e}}$ at its peak point is:

$$\begin{aligned}
\Phi_{\text{mod,e}}(\Delta\theta = 0) &= f_d\frac{R - r_s}{R - r_e} \\
&= \frac{r_e}{r_s}\frac{H_c}{-H_c} \\
&= -\frac{r_e}{r_s} \leq -1 \,.
\end{aligned}$$

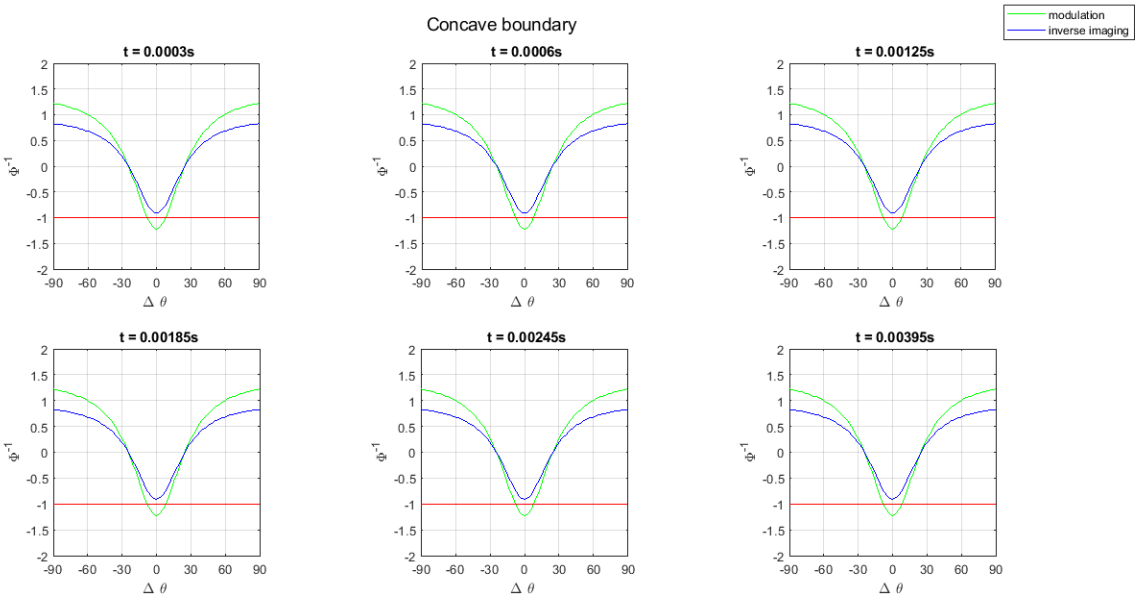

Figure 4.9: Φ^{-1} for concave boundaries. The green curve represents $\Phi^{-1}_{\text{mod, e}}$, and blue curve represents Φ^{-1}_{inv}. The red line represents $\Phi^{-1} = -1$, where perfect reflection takes place.

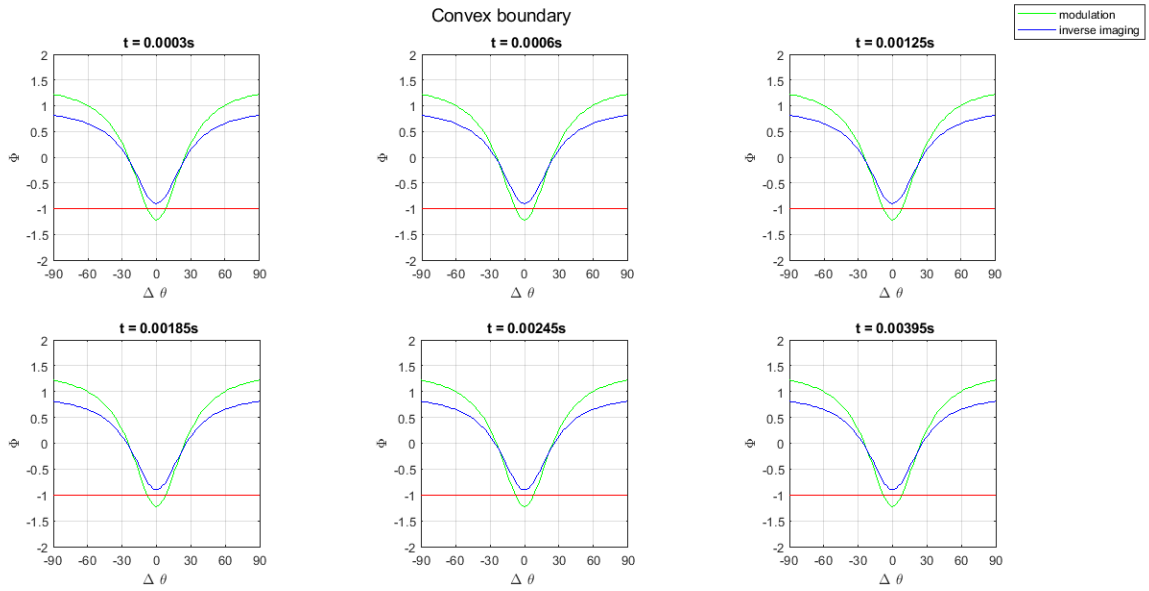

Figure 4.10: Φ for convex boundaries. The green curve represents $\Phi_{\text{mod, e}}$, and blue curve represents Φ_{inv}. The red line represents $\Phi = -1$, where perfect reflection takes place.

5

Conclusions and recommendations

In the previous chapter the smoothness of the boundary flux of inverse imaging was analyzed and compared to the smoothness of the modulated equidistant imaging. The smoothness of the boundary flux in the application of the semi-analytic method for thermal analysis in LBPF is very important, since a smoother curve allows the use of a coarser mesh in the numerical field. Based on the previous chapters a conclusion will be drawn about appropriateness of inverse imaging is for the semi-analytic method compared to modulated equidistant imaging.

5.1. Conclusions

The simulations in the previous chapter showed that the inverse imaging gave a smoother boundary flux than the modulated equidistant imaging, because the reflection of inverse imaging had no fluctuations near the source point, contrary to the reflection of modulated equidistant imaging that did have fluctuations. The absence of fluctuations near the peak flux gave the inverse imaging the advantage to be smoother than modulated equidistant imaging. This was both the case for concave and convex boundaries. The fluctuations in modulated equidistant imaging between partially reflecting and reflecting too much, cause large jumps in the boundary flux. The smoothness of the inverse imaging is mainly caused by the choosing the image point to be at the inverse point, and by the factor γ, which are both inspired by electrostatics. Because the boundary flux of inverse imaging is smoother than modulated equidistant imaging, it requires a courser mesh in numerical implementations to catch the behaviour of the flux. This makes inverse imaging more appropriate to use in the semi-analytic method for the thermal analysis of LPBF-processes.

5.2. Recommendations

For further research the following recommendations can be made:

- The effect of the curvature of the boundary on both equidistant and inverse imaging. Not only the radii of the image points will differ, but also the modulation factor and γ.
- Study the performance of inverse imaging for boundaries that are larger than quarter circles.
- Investigate how inverse imaging performs at elliptical boundaries. Perhaps a coordinate transformation could give similar expressions as expressions for circular boundaries.

6

Appendix

6.1. Temperature contours for a concave boundary

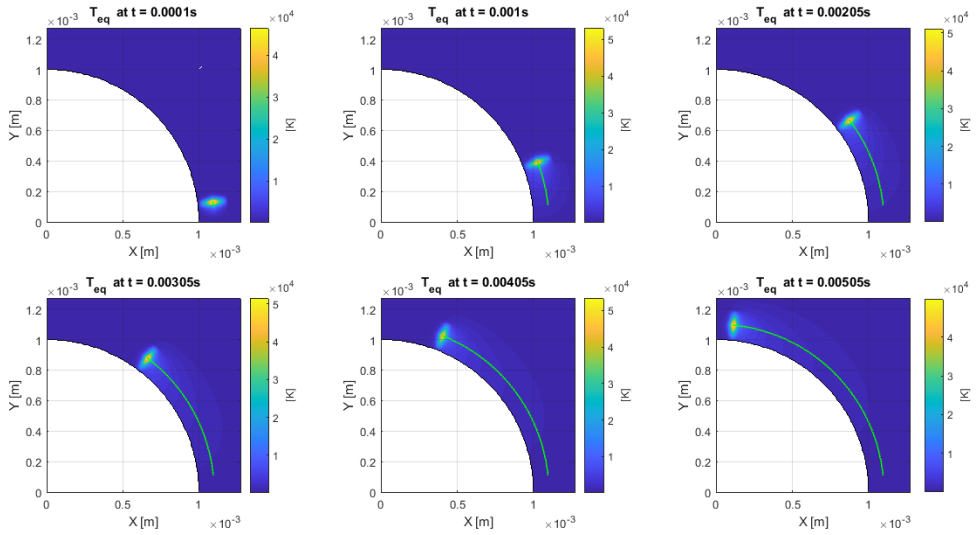

Figure 6.1: The temperature contour plot in a concave boundary for modulated equidistant imaging at chosen time steps during the scanning process. The black arc is the boundary, and the green line is the laser scan.

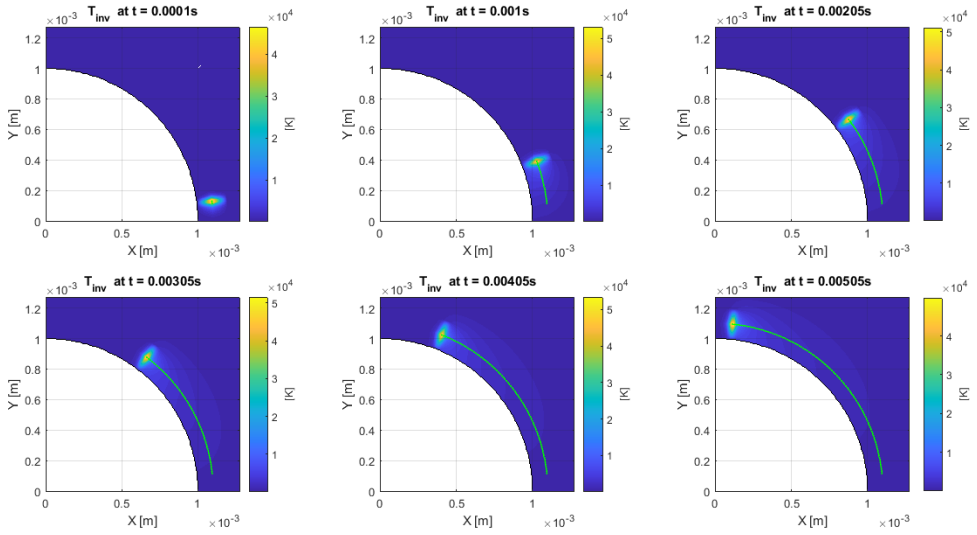

Figure 6.2: The temperature contour plot in a concave boundary for inverse imaging at chosen time steps during the scanning process. The black arc is the boundary, and the green line is the laser scan.

6.2. Temperature contours for a convex boundary

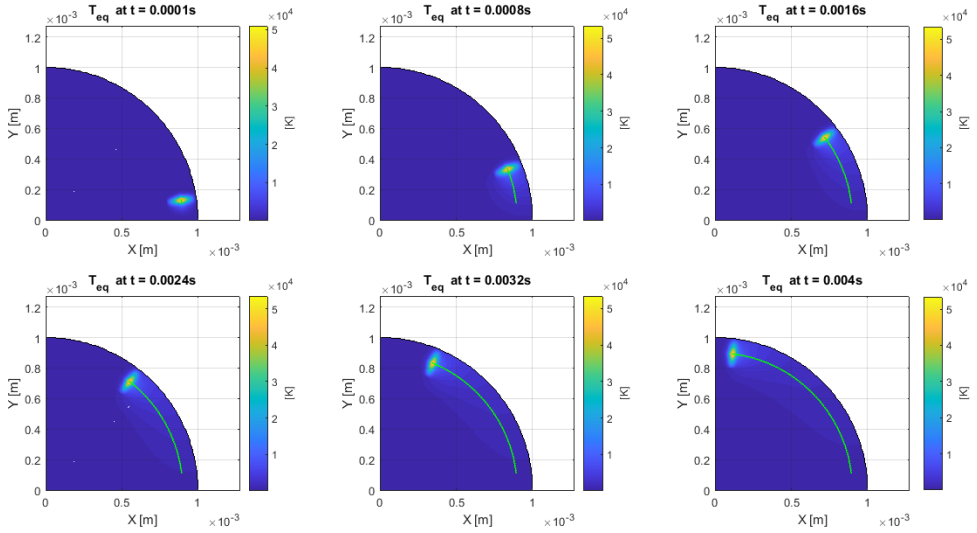

Figure 6.3: The temperature contour plot in a convex boundary for modulated equidistant imaging at chosen time steps during the scanning process. The black arc is the boundary, and the green line is the laser scan.

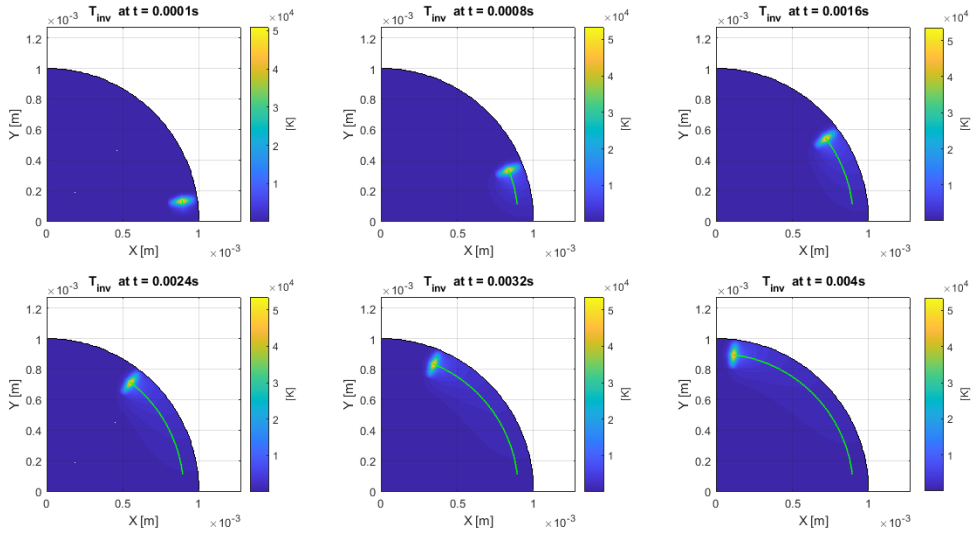

Figure 6.4: The temperature contour plot in a v boundary for inverse imaging at chosen time steps during the scanning process. The black arc is the boundary, and the green line is the laser scan.

7

Bibliography

1. M.E. Zaeh & G. Branner, "Investigations on residual stresses and deformations in selective laser melting," *Production Engineering*, 2010.
2. M.F. Knol, "Thermal modelling of Selective Laser Melting: a semi-analytic approach," *TU Delft*, 2016.
3. Y. Yang, M.F. Knol, F. van Keulen, C. Ayas, "A semi-analytical thermal modelling approach for selective laser melting," *Additive Manufacturing*, 2018.
4. J.C. Steuben, A.J. Birnbaum, J.G. Michopoulus, A.P. Illiopoulus, "Enrinched analytic solutions for additive manufacturing modeling and simulation," *Additive Manufacturing*, 2019.
5. C. Casavola, S. I. Campanelli & C. Pappalettere, "Preliminary investigation on distribution of residual stress generated by selective laser melting process," *Rapid Prototyping Journal*, 2007.
6. E. Yasa & J. Kurth, "Application of laser re-melting on selective laser melting parts," *Advances in Production Engineering & Management*, 2011
7. A. Bandyopapadhyay and Kellen D. Traxel, "Invited review article: Metal-additive manufacturing - Modeling strategies for application-optimized designs," *Additive Manufacturing*, 2018.
8. H.S. Carslaw & J.C. Jeager, "Conduction of Heat in Solids," *Oxford University Press*, 1959.
9. A.F. Mills, "Basic Heat and Mass Transfer," *Pearson Education Limited*, 2014.
10. R. Haberman, "Applied partial differential equations," *Pearson*, 1983.
11. J. van Kan, A. Segal, F. Vermolen, "Numerical Methods in Scientific Computing," *Delft Academic Press*, 2014.
12. C.A. Brebbia & S. Walker, "Boundary Element Techniques in Engineering," *The Butterworth Group*, 1980.
13. J.D. Jackson, "Classical Electrodynamics," *John Wiley & Sons*, 1962.
14. J.H. Jeans, "Mathematical Theory of Electricity and Magnetism," *Cambridge University Press*, 1908.